

High statistics study of the reaction $\gamma p \rightarrow p\pi^0\eta$

The CBELSA/TAPS Collaboration

E. Gutz^{1,2}, V. Crede³, V. Sokhoyan^{1,a}, H. van Pee¹, A.V. Anisovich^{1,4}, J.C.S. Bacelar⁵, B. Bantes⁶, O. Bartholomy¹, D. Bayadilov^{1,4}, R. Beck¹, Y.A. Beloglazov⁴, R. Castelijns⁵, H. Dutz⁶, D. Elsner⁶, R. Ewald⁶, F. Frommberger⁶, M. Fuchs¹, Ch. Funke¹, R. Gregor², A.B. Gridnev⁴, W. Hillert⁶, Ph. Hoffmeister¹, I. Horn¹, I. Jaegle⁷, J. Junkersfeld¹, H. Kalinowsky¹, S. Kammer⁶, V. Kleber^{6,b}, Frank Klein⁶, Friedrich Klein⁶, E. Klempt¹, M. Kotulla^{2,7}, B. Krusche⁷, M. Lang¹, H. Löhner⁵, I.V. Lopatin⁴, S. Lugert², T. Mertens⁷, J.G. Messchendorp⁵, V. Metag³, M. Nanova³, V.A. Nikonov^{1,4}, D. Novinsky^{1,4}, R. Novotny², M. Ostrick^{6,a}, L. Pant^{2,c}, M. Pfeiffer², D. Piontek¹, A. Roy^{2,d}, A.V. Sarantsev^{1,4}, Ch. Schmidt¹, H. Schmieden⁶, S. Shende⁵, A. Süle⁶, V.V. Sumachev⁴, T. Szczepanek¹, A. Thiel¹, U. Thoma¹, D. Trnka², R. Varma^{2,d}, D. Walther^{1,6}, Ch. Wendel¹, A. Wilson^{1,3}

¹Helmholtz-Institut für Strahlen- und Kernphysik, Universität Bonn, Germany

²II. Physikalisches Institut, Universität Gießen, Germany

³Department of Physics, Florida State University, Tallahassee, USA

⁴Petersburg Nuclear Physics Institute, Gatchina, Russia

⁵Kernfysisch Versneller Instituut, Groningen, The Netherlands

⁶Physikalisches Institut, Universität Bonn, Germany

⁷Institut für Physik, Universität Basel, Switzerland

Received: date / Revised version: date

Abstract. Photoproduction off protons of the $p\pi^0\eta$ three-body final state was studied with the Crystal Barrel/TAPS detector at the electron stretcher accelerator ELSA at Bonn for incident energies from the $\pi^0\eta$ production threshold up to 2.5 GeV. Differential cross sections and the total cross section are presented. The use of linearly polarized photons gives access to the polarization observables Σ , I^s and I^c , the latter two characterize beam asymmetries in case of three-body final states. $\Delta(1232)\eta$, $N(1535)1/2^-\pi$, and $pa_0(980)$ are the dominant isobars contributing to the reaction. The partial wave analysis confirms the existence of some nucleon and Δ resonances for which so far only fair evidence was reported. A large number of decay modes of known nucleon and Δ resonances is presented. It is shown that detailed investigations of decay branching ratios may provide a key to unravelling the structure of nucleon and Δ resonances.

1 Introduction

At medium energies, our present understanding of QCD is limited. In the energy regime of meson and baryon resonances, the strong coupling constant is large and perturbative methods cannot be applied. Lattice QCD has made great progress in the calculation of properties of ground-state baryons, and even excited states are being explored [1]. But there is still a long path ahead before the baryon resonance spectrum from the lattice can be considered understood. One of the key issues in this energy regime is therefore to identify the relevant degrees of freedom and the effective forces between them. A necessary step towards this aim is undoubtedly a precise knowledge of the

experimental spectrum of hadron resonances and of their properties.

Quark models are in general amazingly successful in describing the spectrum of known hadronic states. However, in meson spectroscopy, there seems to be an overpopulation: more states are found experimentally than are expected from a $q\bar{q}$ scheme. Intrusion of glueballs, hybrids, multiquark states, and of molecules have been suggested to explain the proliferation of states [2]. However, a conservative approach does not confirm the need for additional resonances [3]. In baryon spectroscopy, the situation is reverse [4]. Due to the three-body nature of the system - which is characterized by two independent oscillators - quark models predict many more resonances than have been observed so far, especially at higher energies [5, 6, 7, 8]. This is the problem of the so-called *missing resonances*. The problem is aggravated by the prediction of additional states, hybrid baryons, in which the gluonic string mediating the interaction between the quarks itself can be excited. Hybrid baryons, if they exist, would in-

^a *Present address:* Institut für Kernphysik, Universität Mainz, Germany

^b *Present address:* German Research School for Simulation Sciences, Jülich, Germany

^c *On leave from:* Nucl. Phys. Div., BARC, Mumbai, India

^d *On leave from:* Department of Physics, IIT, Mumbai, India

crease the density of states at high masses even further; their mass spectrum is predicted to start at 1.8 or 2 GeV [9] or at 2.5 GeV [10]. The properties of some baryon resonances are also difficult to reconcile in quark models. The best known example is the $N(1440)1/2^+$ Roper resonance which is predicted in quark models to have a mass above the negative-parity resonance $N(1535)1/2^-$. The interpretation of the Roper resonance as a dynamically generated object [11] is, however, not supported by recent electroproduction experiments at JLab [12].

High-mass positive and negative parity resonances are often (nearly) degenerate in mass while quark models mostly predict alternating groups of resonances of opposite parity (see, however, also [6,13]). The mass-degeneracy of positive- and negative-parity resonances in both the meson [14] and the baryon [15] spectrum has attracted considerable interest. It has been suggested that in high-mass hadrons, a phase transition may possibly occur causing chiral symmetry to be restored. The constituent-quark mass could evolve in the direction of the current-quark mass [16], and chiral multiplets could be formed: mass-degenerate spin doublets and/or spin and isospin quartets of resonances with identical spin, opposite parity, and similar masses [17, 18, 19].

In ‘‘gravitational’’ theories (AdS/QCD), baryon mass spectra can be calculated analytically [20], and give rather simple results. When confinement is parameterized by a soft wall, the squared masses are just proportional to the sum of the intrinsic orbital angular momentum L and a radial quantum number N [21]. Diquarks which are antisymmetric in spin and flavor - called ‘good diquarks’ by Wilczek [22] - reduce the mass [23]. A two-parameter fit to all baryon masses emerges which reproduces the baryon excitation spectrum with remarkable accuracy [23].

Quarks and gluons may not be the most suitable degrees of freedom to describe hadron resonances. Instead, baryon resonances can be generated dynamically from the interaction of pseudoscalar or vector mesons and ground-state octet or decuplet baryons. In case of pseudoscalar mesons, the meson-baryon interaction is extracted from chiral Lagrangians, from an effective theory of QCD at low energies [24, 25, 26]. For vector mesons, transition amplitudes provided by hidden-gauge Lagrangians can be used to derive an effective interaction [27]. A recent survey of the field can be found in [28]. One might speculate that high-mass resonances could possibly be generated from the interactions between pions and nucleon resonances, or nucleons and meson resonances. To pursue such scenarios, knowledge on cascading decays of baryon resonances are mandatory.

Experimentally, most information on baryon resonances stems from partial wave analyses of πN elastic scattering data performed in the early 80s of the last century [29, 30, 31], even though now a number of new resonances has been reported recently which were deduced from photoproduction data [32]. The resonances predicted but not observed experimentally seem not to be randomly distributed; instead, complete baryon multiplets have remained unobserved [33, 34, 35]. A popular possibility to reduce the num-

ber of predicted resonances is to assume that resonances are formed from a quasi-stable ‘good diquark’ and a third quark [36]. There are two paths to identify the additional degrees of freedom of the three-body dynamics of a full quark model compared to a quark-diquark picture.

i) The number of expected resonances is considerably reduced in quark-diquark models: This was the reason why they were introduced. However, the formation of quasi-stable diquarks seems to be excluded by the existence of a spin-quartet ($S = 3/2$) of positive parity ($L = 2$) nucleon $I = 1/2$ resonances with $J^P = 1/2^+ \dots 7/2^+$ at about 2 GeV [34, 37]: A $L = 2$, $S = 3/2$, $I = 1/2$ wave function is only symmetric when two oscillators - with orbital excitations l_i - are excited, with coherent contributions from excitations with $|L = 2; l_1 = 2, l_2 = 0\rangle$ and $|L = 2; l_1 = 0, l_2 = 2\rangle$, and from simultaneous excitations of both oscillators with $|L = 2; l_1 = 1, l_2 = 1\rangle$. If only one oscillator was excited, the orbital and spin wave functions would be symmetric, the isospin wave function of mixed symmetry, the color wave function is fully antisymmetric, and the full wave function would be incompatible with the Pauli principle.

ii) The excitation of two independent oscillators may lead to changes in the decay pattern. In nuclear physics, the excitation of two nucleons often leads to a step-wise de-excitation of the first, then the second nucleon. Anticipating a result of this paper we may speculate that the $|L = 2; l_1 = 1, l_2 = 1\rangle$ component of the nucleon wave function could prefer decay modes via a cascade, where the intermediate state has negative parity and a wave function with one unit of orbital angular momentum (i.e. a superposition of $|L = 1; l_1 = 1, l_2 = 0\rangle$ and $|L = 1; l_1 = 0, l_2 = 1\rangle$).

2 The reaction $\gamma p \rightarrow p\pi^0\eta$

Multi-body final states can be expected to contribute to the search for missing resonances and are interesting in their own right. In this paper, data on the reaction

$$\gamma p \rightarrow p \pi^0 \eta \quad (1)$$

are studied for photon energies from the $\pi^0\eta$ production threshold up to $E_\gamma = 2.5$ GeV. Compared to the data of the CB-ELSA collaboration reported in [38, 39], the statistics is increased by more than a factor of 12, and the solid angle coverage is improved. In a subsequent paper [40], we discuss the reaction $\gamma p \rightarrow p \pi^0 \pi^0$. Reaction (1) benefits from a strong $\Delta(1232)\eta$ contribution. Here, the η acts as an isospin filter: resonances decaying into $\Delta(1232)\eta$ must have isospin $I = 3/2$. The reaction (1) is hence easier to analyze than $\gamma p \rightarrow p \pi^0 \pi^0$.

The first report [41] on $\pi^0\eta$ photoproduction demonstrated already the power of this reaction for the study of nucleon and, in particular, of Δ resonances. The data indicated that Δ resonances around 1.9 GeV likely contribute to this reaction. This conjecture was confirmed by a partial wave analysis suggesting contributions from six Δ resonances, $\Delta(1600)3/2^+$, $\Delta(1920)3/2^+$, $\Delta(1700)3/2^-$,

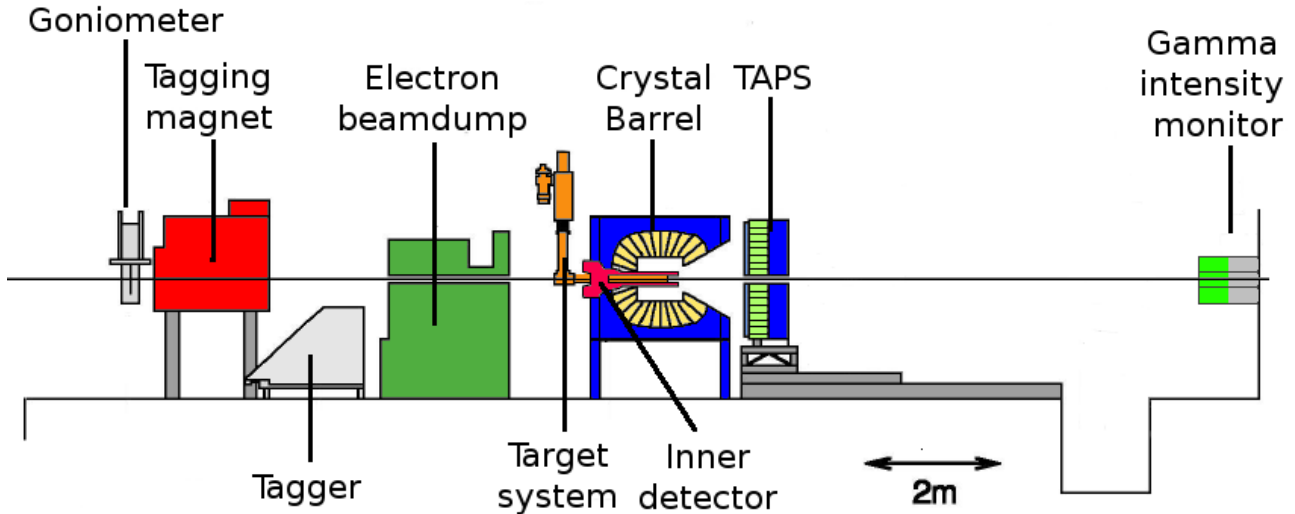


Fig. 1. Schematic picture of the CBELSA/TAPS experiment.

$\Delta(1940)3/2^-$, $\Delta(1905)5/2^+$, $\Delta(2360)3/2^-$, and from two nucleon resonances, $N(1880)1/2^+$ and $N(2200)3/2^+$ [38]. Particularly interesting was the observation of a parity doublet ($\Delta(1920)3/2^+$, $\Delta(1940)3/2^-$) [39], unexpected in quark models [5, 7] and in lattice gauge calculations [1], but predicted [23] by models based on AdS/QCD [42, 43, 44, 45] as well as by the conjecture that chiral symmetry might be restored in excited baryons [15].

The GRAAL collaboration reported results on $\gamma p \rightarrow p\pi^0\eta$ and found that the low energy region is dominated by the formation of $\Delta(1700)3/2^-$ and the sequential decay chain $\Delta(1700)3/2^- \rightarrow \Delta(1232)\eta \rightarrow p\pi^0\eta$ [46]. This result was confirmed by precision data taken with the Crystal Ball/TAPS detector and the tagged photon facility at the MAMI C accelerator in Mainz in the 0.95 – 1.4 GeV energy range [47]. A ratio of the hadronic decay widths $\Gamma_{\eta\Delta}/\Gamma_{\pi N(1535)1/2^-}$ and the ratio $A_{3/2}/A_{1/2}$ of the helicity amplitudes for this resonance were reported.

Polarization observables are important in photoproduction to disentangle the multitude of contributing resonances. In case of photoproduction of single mesons with linearly polarized photons the cross section (equation 19) shows a $\cos 2\phi$ dependence where ϕ denotes the angle between the plane of linear polarization and the reaction plane. In three-body decays the angle can be defined using p , π^0 , or η as reference particle, recoiling against the respective two-particle system. However, additional observables, I^s and I^c , can be extracted due to the fact that an intermediate resonance can be aligned such that its magnetic sub-states do not need to have a statistical population [48]. The alignment leads to an additional dependence of the number of events on the angle between the reaction plane and the decay plane of the three-body final state. The large asymmetries reported in [49] demonstrated the high sensitivity of I^s to the dynamics of the reaction. Further confirmation of the dynamical nature

of the $\Delta(1700)3/2^-$ resonance and its S-wave decay into $\Delta(1232)\eta$ is derived from studies of I^s and I^c in $\gamma p \rightarrow p\pi^0\eta$ [50], within a chiral unitary approach for η - $\Delta(1232)$ scattering [51].

The paper is organized as follows: The experiment is described in section 3, followed by sections 4 on calibration and reconstruction and 5 on data selection. In section 6, we describe the technique how total and differential cross sections and polarization observables are extracted from the data and present the results. An interpretation of the data by means of a partial wave analysis is given in section 7. The paper ends with a short summary in section 8.

3 Experiment and Data

3.1 Overview

The experiment was carried out at the electron accelerator facility ELSA [52] at the University of Bonn using a combination of the Crystal Barrel [53] and TAPS [54, 55] detectors. The experimental setup is shown in Fig. 1.

Electrons with an energy of $E_0 = 3.175$ GeV were extracted from ELSA via slow resonant extraction, impinging on a diamond crystal producing energy-tagged, linearly polarized photons. The photon beam hit a liquid H_2 target. The direction of charged particles produced in a photo-induced reaction could be measured by a three-layer scintillating fiber detector inside the Crystal Barrel or plastic scintillator tiles in front of the TAPS detector, respectively. Charged and neutral particles were detected in the Crystal Barrel or the TAPS detector.

3.2 Photon beam and tagging system

The photon-beam facility at ELSA delivered a tagged photon beam in the energy range from 0.5 to 2.9 GeV. The

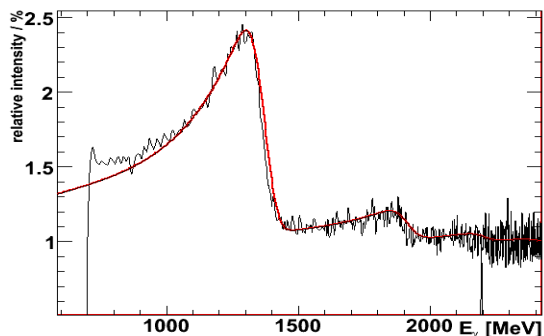


Fig. 2. Relative intensity of coherent bremsstrahlung. The spectrum was obtained with the tagging system and a diamond crystal radiator and normalized to the corresponding incoherent spectrum [56]. The enhancements due to coherent processes are clearly visible. Solid line: ANB calculation [57, 58].

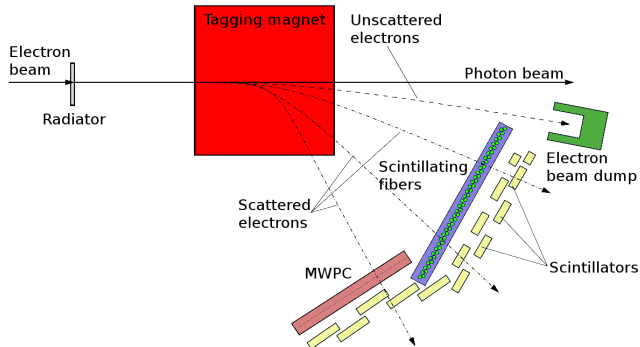


Fig. 3. Schematic view of the tagging system.

primary electron beam of energy E_0 passed either through a thin copper radiator with a thickness of $(3.5/1000) \cdot X_R$ (radiation length) or, alternatively, coherent bremsstrahlung was produced from a $500 \mu\text{m}$ thick diamond crystal, corresponding to $(4/1000) \cdot X_R$. Fig. 2 shows the intensity - normalized to the spectrum of an amorphous copper radiator - as a function of photon energy for a typical setting of the radiator. Technical details are given in [56], the settings for the data presented here are discussed in section 5.1.

Electrons were deflected in the field of the tagger dipole magnet according to their energy loss in the bremsstrahlung process. Electrons not undergoing bremsstrahlung were deflected at small angles and guided into a beam dump located behind the tagging detectors. The beam dump consisted of layers of lead and iron, combined with polyethylene and boron carbide. The beam dump was built in a way to provide shielding of the detector system against possible background produced by the electrons. Nevertheless, there were background contributions in the calorimeters originating from the beam dump. These contributions were suppressed in the offline analysis, based on their unique topology.

The energy E_{e^-} of electrons which have undergone bremsstrahlung was determined in a tagger detector con-

sisting of three components, as can be seen in Fig. 3. The corresponding energy of a bremsstrahlung photon is $E_\gamma = E_0 - E_{e^-}$. A hodoscope of 480 scintillating fibers of 2 mm diameter covered the photon energy range from 18% to 80% of the incoming electron energy. The energy resolution of the hodoscope varied between 2 MeV (low electron energy) and 13 MeV (high electron energy). Highly deflected electrons were detected in a multi-wire proportional chamber (208 wires), covering high-energy photons with 80% to 92% of the incoming electron energy. In the present analysis, these data were not used. Behind the scintillating fibers and proportional chamber, 14 scintillation counters (tagger bars) were mounted in a configuration with adjacent paddles partially overlapping. The scintillator bars were read out by Time-to-Digital Converters (TDC) and Charge-to-Digital Converters (QDC).

3.3 Target and scintillating-fiber detector

The photons hit the liquid hydrogen target in the center of the Crystal Barrel (CB) calorimeter. The cylindrical target cell (52.75 mm in length, 30 mm in diameter) was built from kapton foil of $125 \mu\text{m}$ thickness; at both ends, a $80 \mu\text{m}$ kapton foil was used. The target was positioned in an aluminum beam-pipe, which had a thickness of 1 mm. The target was surrounded by a scintillating fiber detector [59,60], which provided an unambiguous impact point for charged particles leaving the target. The detector was 400 mm long, had an outer diameter of 130 mm and covered the polar angle range of $28^\circ < \theta < 172^\circ$. It consisted of 513 scintillating fibers with a diameter of 2 mm, which were arranged in three layers (see Fig. 4). For the detection of the charged particles, a coincidence between two or three layers of the detector was used. The outer layer (191 fibers) was positioned parallel to the beam axis, the middle layer (165 fibers) was oriented at an angle of $+25.7^\circ$, the innermost (157 fibers) at an angle of -24.5° with regard to the beam axis. The angles resulted from the requirement for the bent fibers to cover exactly halfway around the detector. This arrangement allowed an unambiguous identification of the position of the hits if only two of the fibers were fired. The readout was organized via 16-channel photomultipliers connected to the fibers via light guides. The efficiency of the detection in case of the hits with two overlapping layers was 98.4%, in the case of three overlapping layers 77.6%.

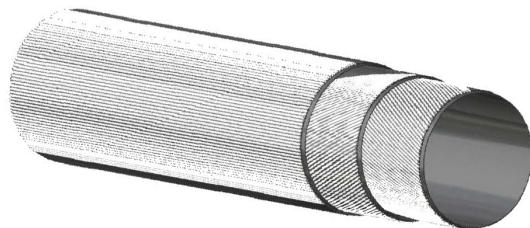


Fig. 4. The inner scintillating fiber detector with three layers comprising a total of 513 fibers.

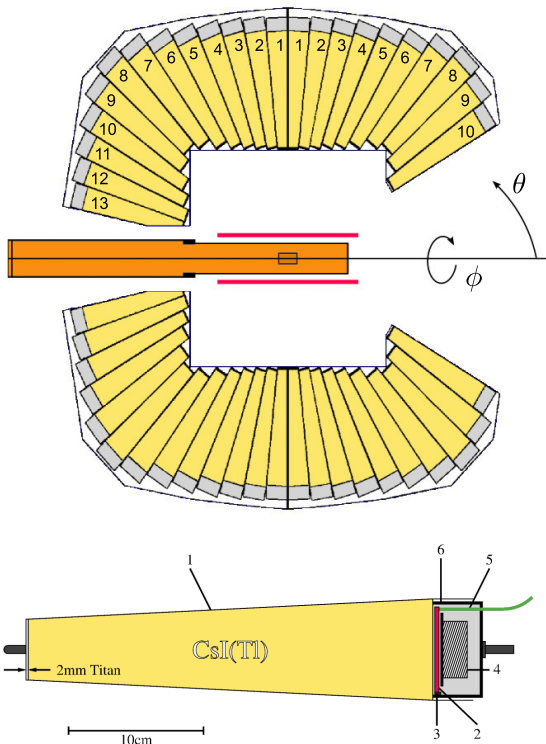


Fig. 5. Top: Schematic view of the Crystal Barrel calorimeter. The photon beam enters from the left. Numbers denote ϕ -symmetric rings of identical module types. Also visible are the position of the inner detector and the LH₂ target cell surrounded by the beam pipe. Bottom: Schematic view of a CsI(Tl) module. 1: Titanium casing, 2: Wavelength-shifter, 3: Photodiode, 4: Preamplifier, 5: Optical fiber, 6: Electronics casing.

3.4 The Crystal Barrel detector

The Crystal Barrel (see Fig. 5) is an electromagnetic calorimeter particularly well-suited for the measurement of the energy and coordinates of photons. In its CBELSA/TAPS configuration of 2002/2003, it consisted of 1290 CsI(Tl) crystals arranged in 23 rings and covered the angular range from 30° to 168° in the polar angle (θ) and the complete azimuthal range (ϕ). Each crystal had a length of 30 cm corresponding to 16.1 radiation lengths [53] and covered 6° both in polar and azimuthal angles. An exception were the crystals in the three backward rings which covered 6° in θ and 12° in ϕ . The energy of the photons inducing showers in the Crystal Barrel was determined via identification of clusters of hit crystals and by summation of the energy deposits in a cluster. Details are given in Section 4.4. The energy resolution of the Crystal Barrel depends on the energy of the photons as [53]:

$$\frac{\sigma(E)}{E} = \frac{2.5\%}{\sqrt[4]{E[\text{GeV}]}}. \quad (2)$$

The spatial resolution of the Crystal Barrel is related to the energy of the photons, and for energies higher than 50 MeV was better than 1.5° if a special weighting algo-

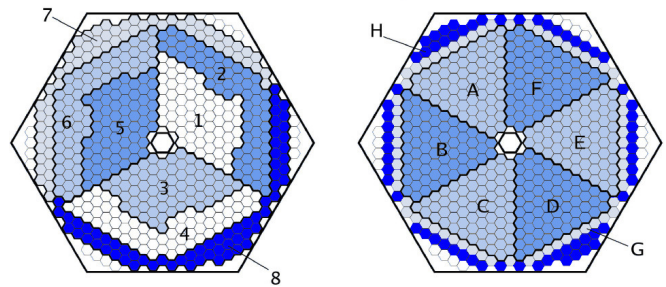


Fig. 6. TAPS trigger segmentation, on the left: segmentation used for the LED low trigger, on the right: the sectors used in the formation of the LED high trigger.

gorithm was used for the determination of the photon position (see Section 4.4). The energy deposit in the crystals of the Crystal Barrel was measured via detection of the scintillation light using PIN photodiode readout. Its wavelength was shifted using a wavelength shifter to longer wavelengths matching the range of the sensitivity of the photodiode. After detection by the photodiode the signal was processed via preamplifier and dual-range ADC readout. To control the functionality of the readout and stability of the calibration, a light-pulsar system was used, feeding light directly into the wavelength shifter. For more details see [61].

3.5 The TAPS detector

The TAPS calorimeter complemented the Crystal Barrel in the forward direction, covering the polar angular range from 30° down to 5.8° and the full azimuthal range. It consisted of 528 hexagonal BaF₂ modules in a forward wall setup, 1.18 m from the target center. A schematic picture of the TAPS crystal assembly and its hexagonal shape is shown in Fig. 6. The forward opening of TAPS allowed for the passage of the photon beam.

The BaF₂ modules used in the TAPS calorimeter have a width of 59 mm and a length of 250 mm, corresponding to 12 radiation lengths. Their cylindrical rear end with a diameter of 54 mm was attached to a photomultiplier. The front end of the crystal was covered by a separate, 5 mm thick plastic scintillator for the identification of charged particles (mounted in a contiguous wall in front of the calorimeter). These *charged particle vetos* [62] were read out via optical fibers connected to multi-anode photomultipliers. The readout of the BaF₂ modules with photomultipliers allowed for signal processing without the use of additional preamplifiers or shapers and could be used not only for energy but also timing information. The signals of each module were split and processed by constant-fraction discriminators (CFDs, see section 4.2) and leading-edge discriminators (LEDs) for trigger purposes as described in the next paragraph.

The combination of the Crystal Barrel and TAPS calorimeters covered 99% of the 4 π solid angle and served as an excellent setup to detect multi-photon final states. For photons up to an energy of 790 MeV, the energy reso-

lution of TAPS as a function of the photon energy is given by [55]

$$\frac{\sigma(E)}{E} = \frac{0.59\%}{\sqrt{E_\gamma}} + 1.91\%. \quad (3)$$

3.6 The Photon Intensity Monitor

The Photon Intensity Monitor consisted of a 3×3 matrix of PbF_2 crystals with photomultiplier readout, mounted at the end of the beam line. It was used to measure the position of the photon beam in the set-up period and to monitor the photon flux by counting the coincidences between the Photon Intensity Monitor and the tagging system.

3.7 The trigger

The purpose of the trigger was to select events in which a tagged photon of known energy induced a hadronic reaction in the target with a minimum number of photons detected in the Crystal Barrel or in TAPS, and to suppress e^+e^- background from the conversion of beam photons. The TAPS modules provided the first-level trigger. A second-level trigger was based on a cellular logic (FACE), which determined the number of clusters in the Crystal Barrel. The trigger required either two hits above a low-energy threshold in TAPS, or one hit above a higher-energy threshold in TAPS in combination with at least one FACE cluster.

First-level trigger: The TAPS crystals were read out with two Leading Edge Discriminator settings, one set at a high threshold (LED high) and one at a low threshold (LED low). The shape of the logical segmentation for the TAPS trigger is shown in Fig. 6. The thresholds have been set ringwise, with values increasing with decreasing polar angle. If two LED low signals from different segments are present, the event was digitized and stored, and the decision of the second level trigger was not required. If at least one TAPS crystal provided a LED high signal, the event was digitized but the decision about its final storage was deferred to the second level trigger.

Second-level trigger: The second level trigger was based on the relatively slow Crystal Barrel signals. Two different trigger settings have been used in the data presented here, demanding one or two clusters to be identified by the cluster-finder algorithm FACE. The processing time varied between $6 \mu\text{s}$ and $10 \mu\text{s}$, depending on the size of the clusters. Accepted events were stored.

4 Calibration and reconstruction

4.1 Crystal Barrel calibration

The calibration of the Crystal Barrel used the position of the π^0 peak in the $\gamma\gamma$ invariant mass spectrum (the recon-

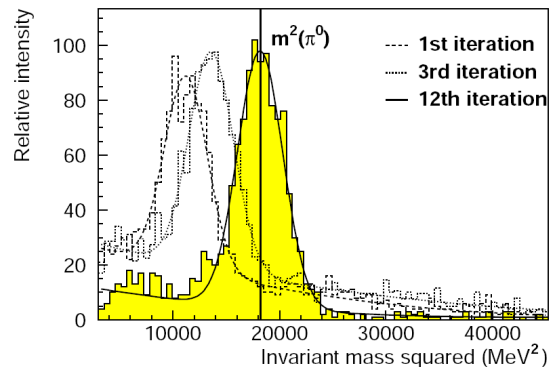


Fig. 7. π^0 peak used for the calibration of one CsI(Tl) module in different iterations of the calibration procedure [63].

struction of γ energies from hits in the Barrel is described below in section 4.4). Fig. 7 shows the invariant mass spectra of photon pairs, one of them hitting a selected crystal, for different iterations. As long as the invariant mass was too low, the assigned photon energy was increased. After all crystals were adjusted, the next iteration was started until the results were stable. The calibration using the π^0 mass was sufficient; no additional correction was required to adjust the η mass. The CB crystals were read out via dual range ADCs. The low ADC range covered the photon energies up to about 130 MeV and was calibrated using the π^0 mass as a reference. The high range of the ADC covered the energies up to about 1100 MeV. The high range was calibrated relative to the low range using a light-pulsar with adjustable attenuations. The light was directly fed into the wavelength shifter of the CsI(Tl) readout, and produced signals with shapes simulating the response of the CB crystals. Using the known gain of the ADC in the low range, the calibration was extended to the high range.

4.2 TAPS calibration

Since the fast photomultiplier readout of the TAPS calorimeter allowed for timing signals to be branched off, TAPS required a timing calibration as well as an energy calibration.

Time calibration: Two steps were done for the time calibration of TAPS: calibration of the gain and calibration of the time offsets of the TAPS TDC modules. The gain of the TAPS TDC modules was calibrated using pulses with known repetition frequencies, and by variation of the pulse frequency. The TDC time offsets (due to different cable lengths) were calibrated using the time differences between two neutral hits detected in TAPS, belonging to the same π^0 decay. Fig. 8 shows the distribution of the timing differences of different TAPS modules after calibration. The time resolution was determined to $\sigma = 0.35 \text{ ns}$.

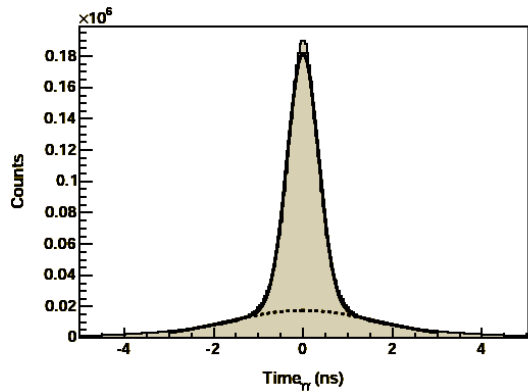


Fig. 8. Time difference between hits in the TAPS crystals. The crystals for which the time difference was within the grey area were considered as parts of the same cluster, taken from [64].

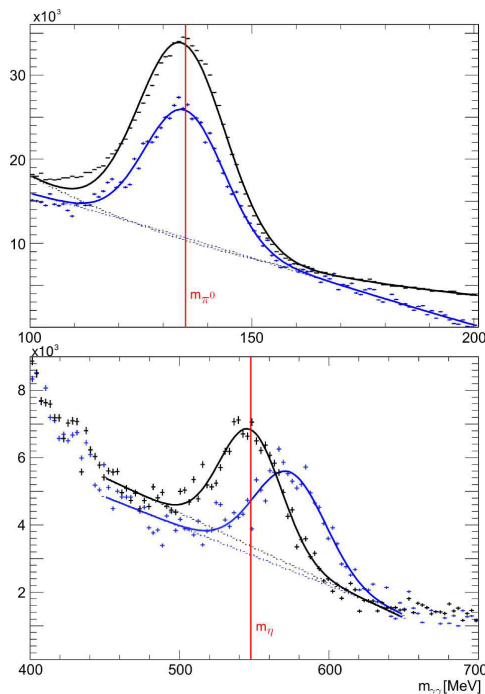


Fig. 9. Effect of the energy-dependent calibration (TAPS). Reconstructed π^0 - (top) and η -mass (bottom) before (blue) and after (black) application of the correction function (4) (using different data samples, counts refer to uncorrected spectra).

Energy calibration: The energy calibration of TAPS was performed in three steps: using cosmic rays, the invariant mass of the photons from π^0 decays, and using the invariant mass of the photons from η decays. Cosmic-ray muons deposit an average energy of 38.5 MeV in the 59 mm wide TAPS crystals. The energy offset was determined using electronic pulses of minimum pulse height. The positions of the minimum ionizing peak and of the pedestal peak obtained with the pulser determined a first approximate calibration of the charge-to-digital converters using a linear function. In a second step, the invariant mass of the two photons originating from π^0 decays - with one pho-

ton hitting crystal i as central crystal of a cluster - was compared to the nominal π^0 mass, and a gain correction was applied to the energy of crystal i . This procedure was performed iteratively until the distribution of invariant masses of photon pairs reproduced the π^0 mass. The result of this calibration is shown in Fig. 9, top. Good agreement between the calculated invariant mass and the nominal π^0 mass was achieved.

Photons from η decays were used in a third step. Of course, here the statistics was comparatively low. Therefore an overall correction gain factor was determined only. The correction function was applied in the form:

$$E_{new} = a \cdot E_{old} + b \cdot E_{old}^2, \quad (4)$$

where the coefficients a and b were determined so that both measured masses, the π^0 and η mass, coincided with the nominal values. Typical values for the coefficients were $a = 1.0165$, $b = -5.6715 \cdot 10^{-5}$. Fig. 9 shows the effect of the correction of the invariant mass on two photons using Eq. 4.

4.3 Tagger calibration

Time calibration: The time of the fibers of the tagger hodoscope relative to the TAPS timing was measured by time-to-digital converters. Fig. 10 shows the distribution of the time differences of fiber signals and signals in TAPS after calibration. A tagger time resolution of better than $\sigma = 1$ ns was deduced.

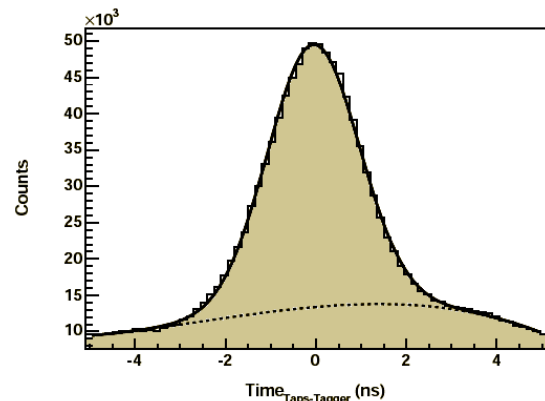


Fig. 10. Calibrated relative timing between the tagging hodoscope and TAPS, taken from [64].

Energy calibration: Electrons hitting one of the fibers of the tagging hodoscope have been deflected in the field of the tagger magnet. For electrons which have passed the radiator, each fiber defined a small range of energies. To determine the energy of electrons as a function of the hit fiber, the relation between the energy of the electron and the fiber number was calculated from the known geometry

and the known magnetic field map, resulting in a fifth degree polynomial. This polynomial was then corrected using the direct injection of electrons with four different energies (680, 1300, 1800, and 2500 MeV) at a constant field of the tagging dipole of 1.413 T. The final polynomial used in this work is given by

$$E = 2533.81 - 190.67 \cdot 10^{-2}x \quad (5) \\ + 28.86 \cdot 10^{-4}x^2 - 34.43 \cdot 10^{-6}x^3 \\ + 95.59 \cdot 10^{-9}x^4 - 12.34 \cdot 10^{-11}x^5,$$

where E is the photon energy and x the fiber index (see Fig. 11).

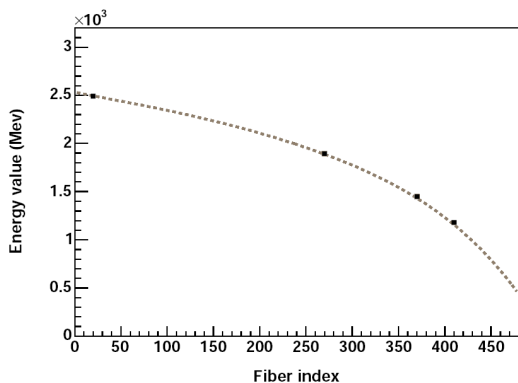


Fig. 11. Relation between photon energy and fiber number. Dashed line: Tagger polynomial (5), points: Data obtained by direct injection.

4.4 Reconstruction

In this section we discuss how kinematic variables like energies and momenta were calculated from the detector information using various reconstruction routines.

Crystal Barrel reconstruction: The reconstruction of photons in the Crystal Barrel detector was performed in the same way as described in [65], forming clusters of contiguous CsI(Tl) crystals with individual energy deposits above 1 MeV and an energy sum of at least 20 MeV to reduce the contributions from split-offs, separate clusters of energy, which might have originated from fluctuations of the electromagnetic shower induced by photons. If there was only one local maximum in the cluster, the energy measured by the participating crystals i was added directly to get the *Particle Energy Deposit* (PED)

$$E_{\text{PED}} = E_{\text{cl}} = \sum_i E_i, \quad (6)$$

where E_{cl} is the cluster energy. There may be, however, two or more local maxima (central crystals k) in one cluster. Then, the sum of energy contents of each of the central

crystals and its eight neighbors, the *nine-energy* E_9 , was formed

$$E_9^k = E_{\text{cen}}^k + \sum_{j=1}^8 E_j^k, \quad (7)$$

and the total cluster energy was shared accordingly,

$$E_{\text{PED}}^i = \frac{E_9^i}{\sum_k E_9^k} \cdot E_{\text{cl}}. \quad (8)$$

If a crystal i was adjacent to several (j) local maxima, its energy contribution to the nine-energies E_9^i was shared proportional to the energy deposits in the central crystals. For central crystal k , the fraction reads

$$E_{9k,\text{frac}}^i = \frac{E_{\text{cen}}^k}{\sum_j E_{\text{cen}}^j} \cdot E_k^i, \quad (9)$$

where the summation extends over the j adjacent local maxima.

Some loss of the shower energy was unavoidable due to edge effects and some inactive material like the aluminum holding structure of the Crystal Barrel.

A θ -dependent correction function to the PED energy improved the energy resolution:

$$E_{\text{PED}}^{\text{corr}} = \left(a(\theta) + b(\theta) \cdot e^{-c(\theta) \cdot E_{\text{PED}}} \right) \cdot E_{\text{PED}}. \quad (10)$$

The parameters were determined using Monte Carlo simulations, with typical values of $a \approx 1.05$, $b \approx 0.05$, $c \approx 0.007$.

The position of PEDs in the Crystal Barrel calorimeter was determined by a weighted average of the polar and azimuthal angles of the crystal centers, θ_i and ϕ_i ,

$$\theta_{\text{PED}} = \frac{\sum_i w_i \theta_i}{\sum_i w_i}, \quad \phi_{\text{PED}} = \frac{\sum_i w_i \phi_i}{\sum_i w_i}, \quad (11)$$

where the factors w_i are defined as

$$w_i = \max \left\{ 0; W_0 + \ln \frac{E_i}{\sum_i E_i} \right\}, \quad (12)$$

with a constant $W_0 = 4.25$. In case of multi-PED clusters, only the central crystal and its direct neighbors were used for the position reconstruction, so the sum over all crystal energies, $\sum_i E_i$, in (12) was replaced by the nine-energy (7).

A spatial resolution for photons of $1^\circ - 1.5^\circ$ in θ_{lab} and ϕ_{lab} , depending on the energy and polar angle of the incident photon, was achieved. A shower depth correction (see below) was not necessary since all crystals point to the center of the target.

TAPS reconstruction: The energies and the coordinates of the photons in TAPS were determined in a way similar to the Crystal Barrel described above. Here, a cluster was defined as any contiguous group of BaF₂ crystals

registering an energy deposit above their CFD threshold. The hardware thresholds were set to 10 MeV. Again, the crystal with the largest energy deposit within the cluster was taken as the central crystal. The times of the central crystal and other crystals in the cluster were compared to reject contributions from other clusters, not correlated in time; a time window of 5 ns was chosen (see Fig. 8). The total energy of the cluster had to exceed 25 MeV. This cut reduced the probability of fake photons due to split-offs. However, for the polarized data a software value of 30 MeV was used for both, the CFD threshold and the maximum cluster energy, to avoid ϕ dependent systematic effects due to drifts. Due to the geometry of the TAPS calorimeter, the position of the photons was calculated using the cartesian coordinates of the crystals which formed the cluster, again with energy-dependent weighting factors [64]:

$$X = \frac{\sum_i w_i x_i}{\sum_i w_i}, \quad Y = \frac{\sum_i w_i y_i}{\sum_i w_i}, \quad (13)$$

where the factors w_i are defined as in eq. (12), with a constant $W_0 = 4.0$. Since the crystals were mounted in a plane and photons originating from the target developed a shower within the crystals, the center of the shower had a displacement (in the outer direction) which increased with penetration depth and hence with the photon energy. This effect was accounted for by a shift of the reconstructed impact point, s , (on the crystal surface) of

$$\frac{\Delta X}{X} = \frac{\Delta Y}{Y} = \left(\frac{s}{Z} + 1\right)^{-1}; \quad Z = X_0 \left(\ln \frac{E}{E_c} + C_\gamma\right), \quad (14)$$

with $C_\gamma = 2.0$ as determined via Monte Carlo simulations. X_0 is the radiation length of BaF₂, E the photon energy and $E_c = 12.78$ MeV is the critical energy for BaF₂. The resolution in the polar angle was determined to be better than 1.3°.

Inner detector reconstruction: A charged particle traversing the fiber detector could fire one or two adjacent fibers in each layer forming a *British-flag*-like pattern which defined the impact point (see Fig. 12, left). A single charged particle may also fake three intersection points (see Fig. 12, middle). In order not to lose these events, up to three

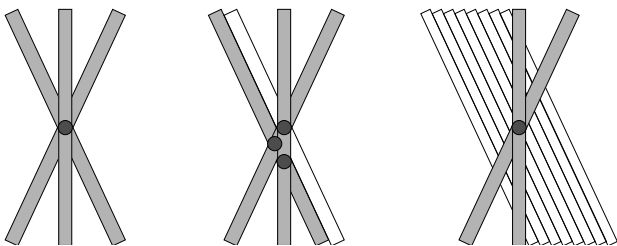


Fig. 12. Charged particles crossing the inner fiber detector produce different hit patterns. A hit in three layers may result in one unique intersection point (left) or in three intersection points (middle). One inefficiency still yields a defined intersection point (right).

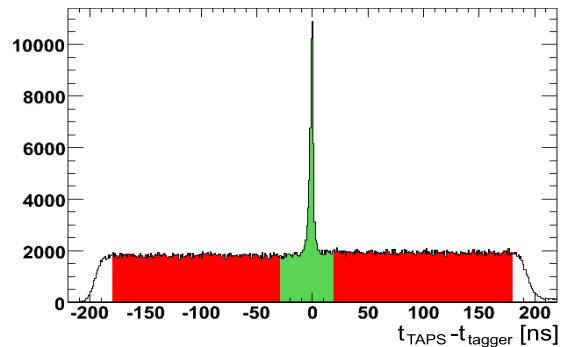


Fig. 13. TAPS-tagger time spectrum. Background events in the signal region (green) were accounted for by sideband subtraction using events from the uniform part in the random background region (red). The signal region was chosen asymmetrically to account for timing signals produced by protons in the TAPS calorimeter.

intersection points were accepted in the reconstruction. One inefficiency (one broken or missing fiber) leading to a pattern shown in Fig. 12, right, was accepted by the reconstruction routine. The accuracy of the reconstruction of the impact point was studied using simulations and was determined, for a pointlike target, to ± 0.5 mm in the X - and Y -coordinates (representing the resolution in ϕ). The uncertainty in the Z coordinate was determined to be 1.6 mm. The angular resolution was $\Delta\phi = 0.4^\circ$ and up to $\Delta\theta = 0.1^\circ$.

Tagger reconstruction Electrons hitting the tagger could fire one or more fibers. In case of more than one fiber hit, contiguous groups of tagger fibers forming clusters were identified. Afterwards the fiber numbers were averaged, and the mean value was used to calculate the electron energy, see Eq. (5). The time of the cluster was taken to be the mean time of the fibers participating in the cluster. For fibers combined to one cluster, a 2 ns time window was imposed. To account for inefficiencies, a group of fibers was still considered as a cluster when one fiber in between two fired fibers had no signal.

Coincidences between tagger and TAPS were imposed in the offline analysis to maintain control of random coincidences. The distribution of time differences of tagger and TAPS hits, $t_{\text{TAPS}} - t_{\text{tagger}}$, is shown in Fig. 13. The peak around 0 ns corresponds to the coincident hits, the evenly distributed events to the uncorrelated accidental background. The coincidence region was selected with a (-30, 20) ns wide cut. The cut is asymmetrical to accept events with slow protons which may have triggered TAPS. The remaining random background under the coincidence peak was subtracted using events in the sidebands, scaled accordingly.

4.5 Monte Carlo simulations

The performance of the detector was simulated in GEANT-3-based Monte Carlo studies. The program package used for CBELSA/TAPS is built upon a program developed for

the CB-ELSA experiment. The Monte Carlo program reproduces accurately the response of the TAPS and Crystal Barrel crystals when hit by a photon. For charged particles, the detector response is reasonably well understood. The bremsstrahlung process, the tagger, and the emerging photon beam are not simulated; the experimental data are taken as input. The hadronic reactions under study are produced by an event generator according to the available phase space. Dynamical effects, like the formation of resonant states, are not simulated. The created particles are tracked through the insensitive material and the detector components in small steps and their interactions calculated on a statistical basis. Possible processes include ionization, Coulomb-scattering, shower formation and decays. The results of the simulation are then digitized based on the properties of the sensitive detector components and stored in the same format as real experimental data, allowing for the use of the same analysis framework for data and simulation. Additionally, the Monte Carlo data has also been subjected to a trigger simulation (see section 3.7). For the reaction discussed here, $\gamma p \rightarrow p\pi^0\eta$, in total 3 million Monte Carlo events were used. These events served to understand possible background contributions as well as the acceptance and reconstruction efficiency.

5 Data and data selection

5.1 Data

Polarization data have been acquired in two different run periods in 2003, referred to as (a) and (b). Both datasets were taken with a diamond crystal to produce linearly polarized bremsstrahlung. The coherent edges for (a) and (b) were set to achieve maximal polarization of 49.2% at $E_\gamma = 1300$ MeV (a) or 38.7% at 1600 MeV (b), respectively. These data were divided into three groups (B), (C), and (D), as indicated by the vertical lines in Fig. 14. Set (B) used the setting (a), restricted to the photon beam energy range $E_\gamma = 970 - 1200$ MeV, set (D) used setting (b) for $E_\gamma = 1450 - 1650$ MeV, and set (C) used data from (a) and (b) in the overlap region, $E_\gamma = 1200 - 1450$ MeV. These data are presented in section 6.6.

For the extraction of total and differential cross sections as well as Dalitz plots, shown in sections 6.1 to 6.4, an incoming photon energy range from threshold up to 2.5 GeV has been selected (A in Fig. 14). However, due to normalization issues, only parts of the May dataset could be used for the extraction of cross sections. These data will be referred to as data set CB/TAPS1. Additionally, data taken in a run period in October and November 2002, using unpolarized photons, is presented and referred to as data set CB/TAPS2.

5.2 Selection

In the following, the selection process for the dataset CB/TAPS1 is explained in detail. In case of the CB/TAPS2 dataset, a slightly different method was applied and is

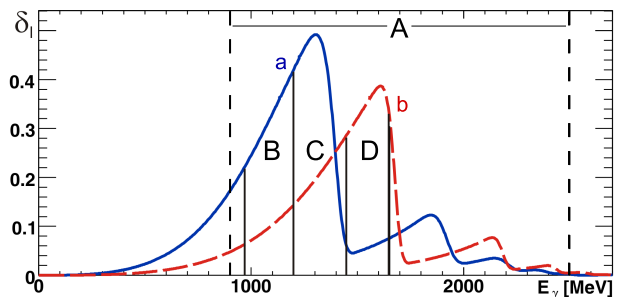


Fig. 14. The degree of linear polarization for the two beam times, (a) and (b). The calculation relies on an Analytic Bremsstrahlung Calculation and on measured photon intensity distributions like the one shown in Fig. 2. The highest polarizations were 49.2% at $E_\gamma = 1305$ MeV (a, March) and 38.7% at 1610 MeV (b, May), respectively (see [56] for details). Vertical lines indicate the energy ranges chosen for the extraction of cross sections (A, CB/TAPS1, May only) and polarization observables (B, C, D), respectively.

addressed in a concluding paragraph. The data selection aims to identify events due to reactions $\gamma p \rightarrow p\pi^0\pi^0$ and $\gamma p \rightarrow p\pi^0\eta$, both with four photons and one proton in the final state. The initial state of the reaction was completely known kinematically (incoming photon momentum, proton mass and momentum), so it was generally possible to reconstruct the final state even if one of the particles escaped detection. This option was not used however, since the contribution of such 4-PED events was found to be negligible. A cut on not more than one charged cluster was applied on the data. Events with all five calorimeter hits marked as neutral were, however, admitted to avoid systematic effects caused by non-uniform charge identification efficiencies of the relevant subdetectors. If five clusters of energy deposits were detected, each of them was then tentatively treated as a proton candidate. The four photons were grouped pairwise to find π^0 and η candidates. The assignment of the observed clusters of energy deposits to protons and π^0 and η mesons was the aim of the combinatorial analysis.

Kinematic cuts: After the preselection of the data detailed above, a combinatorial analysis with respect to the relevant kinematical constraints of the reaction under consideration was performed in order to ascertain the final state particles. Since no proton identification on detector level has been used, each event entered the analysis-chain five times, each time with a different cluster tested against the hypothesis of being the final-state proton.

The coplanarity of a three-body final state poses constraints on the angles between the proton candidate and the remaining four-photon system. In case of the azimuthal angle, the difference $\Delta\phi = \phi_{4\gamma} - \phi_p$ had to agree with 180° within $\pm 10^\circ$. For the polar angle, the different resolutions of the CB and TAPS calorimeters were taken into account in such a way that the difference between the angle of the missing proton calculated from the 4γ -system and the measured fifth cluster, $\Delta\theta = \theta_p^{miss} - \theta_p^{meas}$, had

Variable	Fit function	Mean [MeV]	σ [MeV]	Cut width
Miss. mass	G+pol(3)	936.4	31.8	± 123.6 MeV
$m(\gamma\gamma), \pi^0$	G+pol(3)	135.3	8.6	± 33.6 MeV
$m(\gamma\gamma), \eta$	G+pol(1)	548.2	20.9	± 81.4 MeV
$\Delta\phi$	—	$\pm 180^\circ$	—	$\pm 10^\circ$
$\Delta\theta$	—	0°	—	$\pm 15^\circ$ (CB) $\pm 5^\circ$ (TAPS)

Table 1. Width of the kinematic cuts.

not to exceed $\pm 15^\circ$ for the fifth cluster being detected in the Crystal Barrel, and $\pm 5^\circ$ in TAPS, respectively.

As for the additional constraints posed by the known masses of the final state particles, the corresponding distributions have been fitted assuming a Gaussian signal on a polynomial background. The half-width of the respective cuts has been set to 3.89 times the σ of the Gaussian, translating to a net loss of signal of not more than 10^{-4} or a confidence interval of 99.99%. The corresponding numbers are given in Table 1.

It is unlikely, yet possible, for an event to pass these cuts in more than one combination of final state particles. To eliminate any residual combinatorial background due to such ambiguities in the proton determination, the preselected data were subjected to a preliminary kinematic fit to the $p\pi^0\eta$ final state, described below. Here the only condition to be met is the convergence of the fit. In case of an event passing through this stage multiple times, only the one with the highest confidence level (CL) was retained.

Fig. 15 shows the invariant mass of one $\gamma\gamma$ -pair versus the invariant mass of the other, after the application of the selection procedure described above. Clear signals for both the dominant production of $2\pi^0$ as well as for $\pi^0\eta$ production are observed.

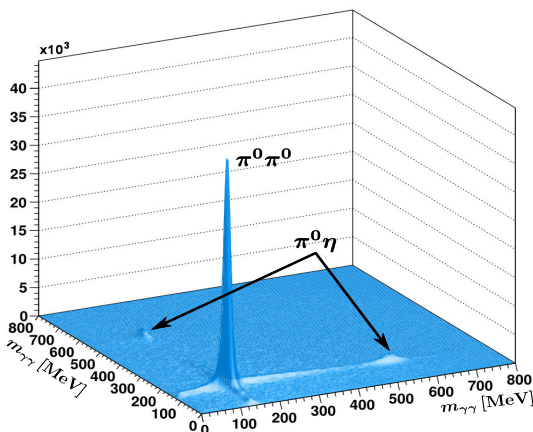


Fig. 15. $\gamma\gamma$ invariant masses after selection of the $p4\gamma$ final state, before kinematic fitting. Cuts on the meson masses have not yet been applied.

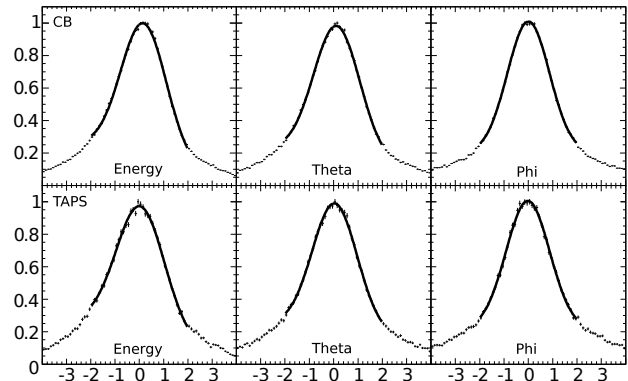


Fig. 16. Pull distributions from the $\gamma p \rightarrow p_{\text{miss}}\pi^0\eta$ fit to the data over the full energy range analyzed. Top row: Particles in the Crystal Barrel, bottom row: Particles in TAPS. Left to right: Pulls in energy, θ , ϕ . The data are well compatible with the expected Gaussian shape with mean $\mu = 0$ and $\sigma = 1$.

Kinematic fits: After the preselection described above, the remaining data sample was subjected to a kinematic fit, imposing energy and momentum conservation as well as the masses of final-state particles as constraints. Analogous to the selection procedure prior to the fit, the proton was treated as a missing particle.

Only a brief description of the fit is given here, for a detailed description of the procedure, see [65]. The kinematic fit used the measured parameters of the reaction and varied them within given error-margins to satisfy the given constraints. The method, apart from improving accuracy by returning corrected quantities, provided means to control the data with respect to systematic effects. The deviations between the measured values used in the fit, e.g. energies and angles of the particles, and the results of the kinematic fit, normalized to the respective measurement errors, should form a Gaussian centered around zero and with unit width (σ). Such so-called *pull*-distributions are shown in Fig. 16, separately for particles detected in one of the two calorimeters for the quantities energy, θ and ϕ , and for the fit hypothesis $\gamma p \rightarrow p_{\text{miss}}\pi^0\eta$ (see below). The presence of systematic effects in the data, not accounted for in the error margins given to the fit, should cause a shift of the distribution. A wrong estimation of the error margins themselves would lead to the width deviating from unity. The distributions were obtained from a fit to the data over the full energy range under consideration and nicely agree with the expected values.

A convenient value to quantify the quality of the fit is the so-called *confidence level* (CL), the integral over the χ^2 probability, varying between 0 and 1. For correctly determined errors, this distribution should be flat. However, background events, leading to bad fits and therefore high χ^2 , should result in a peaking of the CL distribution towards 0. This can be seen in Fig. 17, where the CL distributions for the $\gamma p \rightarrow p_{\text{miss}}\pi^0\eta$ fit hypothesis are shown for data and Monte Carlo simulations. The generally flat distributions show a steep rise towards 0, indicating background contributions in the data or efficiency effects in the reconstruction for some subset of the data and Monte

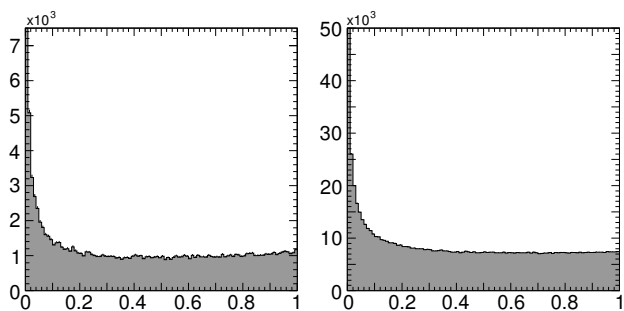


Fig. 17. Confidence level distributions for the hypothesis $\gamma p \rightarrow p_{\text{miss}}\pi^0\eta$, imposing energy and momentum conservation and additionally using the meson masses as constraints. The final state proton is treated as a missing particle. Left: Data, right: Monte Carlo.

Carlo (the MC has been generated background-free). To avoid contamination of the final data sample by such effects, a cut on the CL can be applied.

In the given analysis, the preselected data have been subjected to four differently constrained fits:

$$\gamma p \rightarrow p_{\text{miss}} 4\gamma \quad (15)$$

$$\gamma p \rightarrow p_{\text{miss}} \pi^0 2\gamma \quad (16)$$

$$\gamma p \rightarrow p_{\text{miss}} \pi^0 \pi^0 \quad (17)$$

$$\gamma p \rightarrow p_{\text{miss}} \pi^0 \eta. \quad (18)$$

Here p_{miss} denotes that the proton, identified in the preceding selection, was treated as a missing particle. The first two hypotheses, introducing one and two constraints, respectively, were used for control purposes and background studies only. The latter two hypotheses include energy and momentum conservation and two mass constraints. Convergent fits could be observed for the $\pi^0\pi^0$ hypothesis, some with high confidence levels, even after the selection of the $p\pi^0\eta$ final state described above. Few events fulfilled both the $\pi^0\pi^0$ as well as the $\pi^0\eta$ hypothesis with CLs up to 1. Therefore not only a cut on the CL of the desired reaction, $\text{CL}_{\pi^0\eta} > 0.06$, but also an anticut

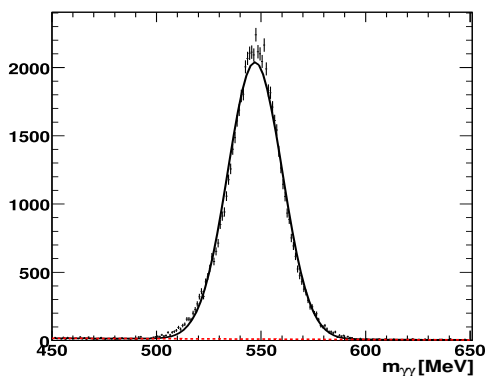


Fig. 18. Invariant mass of the free $\gamma\gamma$ -pair after the $\gamma p \rightarrow p_{\text{miss}}\pi^0\gamma\gamma$ fit, from threshold up to $E_\gamma = 2500$ MeV. An anticut on the $\pi^0\pi^0$ -hypothesis has been performed. The cut on the $\pi^0\eta$ -CL rejects most of the background (dashed line).

on the CL of the competing reaction, $\text{CL}_{\pi^0\pi^0} < 0.01$ has been applied to the data.

Finally, a cross-check between the results of the kinematic fit and the initial selection procedure was performed by comparing the azimuthal and, again independently for the two calorimeters, polar angles of the proton identified at the two stages. Cuts on $\Delta\phi = \pm 4^\circ$, $\Delta\theta_{\text{CB}} = \pm 5^\circ$ and $\Delta\theta_{\text{TAPS}} = \pm 2^\circ$ have been applied to reduce the effects of events, in which the fit had to overly adjust the proton direction, since this might affect the results with respect to the extraction of beam asymmetries.

The final event sample comprised a total of approx. 65,500 events for the extraction of polarization observables and, in two data taking periods, approximately 40,000 (CB/TAPS1 using polarized photons) and 145,000 (CB/TAPS2 using unpolarized photons) for the cross sections and Dalitz plots. In both cases, the final background contamination, derived from the η -signal using different cuts on the kinematic fit and confirmed by comparison to the Monte Carlo simulations (see Fig. 18), amounted to $\approx 1\%$.

Data with unpolarized photons For the CB/TAPS2 data set, the selection procedure was nearly identical to the one described above. Here, however, the proton was allowed to be missing. Again, the contribution of 4-PED events was found to be negligible. Charged and neutral particles were identified using the information from the inner detector and the TAPS vetos, since cross sections are less sensitive to small variations in the charge identification. Each pre-selected event was subjected to the kinematic fit once. As for the tagger reconstruction, each fiber hit in the tagging detector was treated as an individual photon, clustering of fibers was not applied. The selection of the unpolarized data follows the procedure discussed in [66].

6 Extraction of observables

6.1 The total cross section

Fig. 19 shows the total cross section for reaction (1). The cross section is determined from a partial wave analysis to the data described below. The partial wave analysis allows us to generate a Monte Carlo event sample representing the “true” physics. For any distribution, the efficiency can then be calculated as fraction of the reconstructed to the generated events. The open circles in Fig. 19 are given by the number of events, normalized to the incoming photon flux, divided by the efficiency. The red and blue open circles represent the two run periods, CB/TAPS1 and CB/TAPS2, respectively. For CB/TAPS1, the E_γ range covering the coherent peak (b) showed an ($\approx 10\%$) excess of the cross section compared to CB/TAPS2. The data are omitted from further analysis.

The cross section as determined by us is smaller by about 15% compared to those measured at GRAAL [46] and at MAMI [47]. This is particularly intriguing since the cross section for the related reaction $\gamma p \rightarrow p\pi^0\pi^0$ [40] determined from the same data agrees very well with the

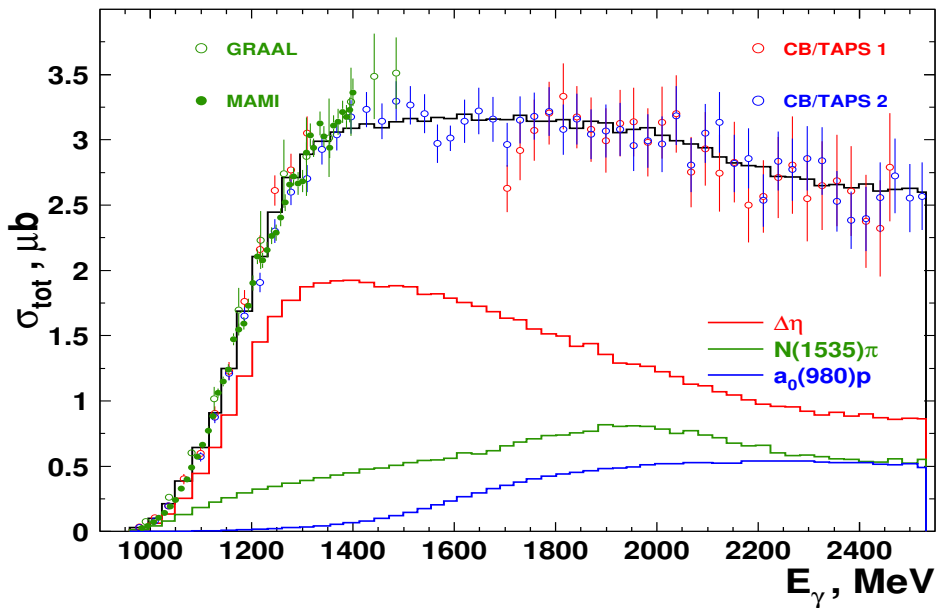


Fig. 19. Total cross sections for the reaction $\gamma p \rightarrow p\pi^0\eta$ (normalized to the MAMI data, see text) and excitation functions for the most important isobars according to the BnGa PWA fits. This work (open circles, blue/red), compared to measurements from GRAAL [46] (open circles, green) and MAMI [47] (full circles, green).

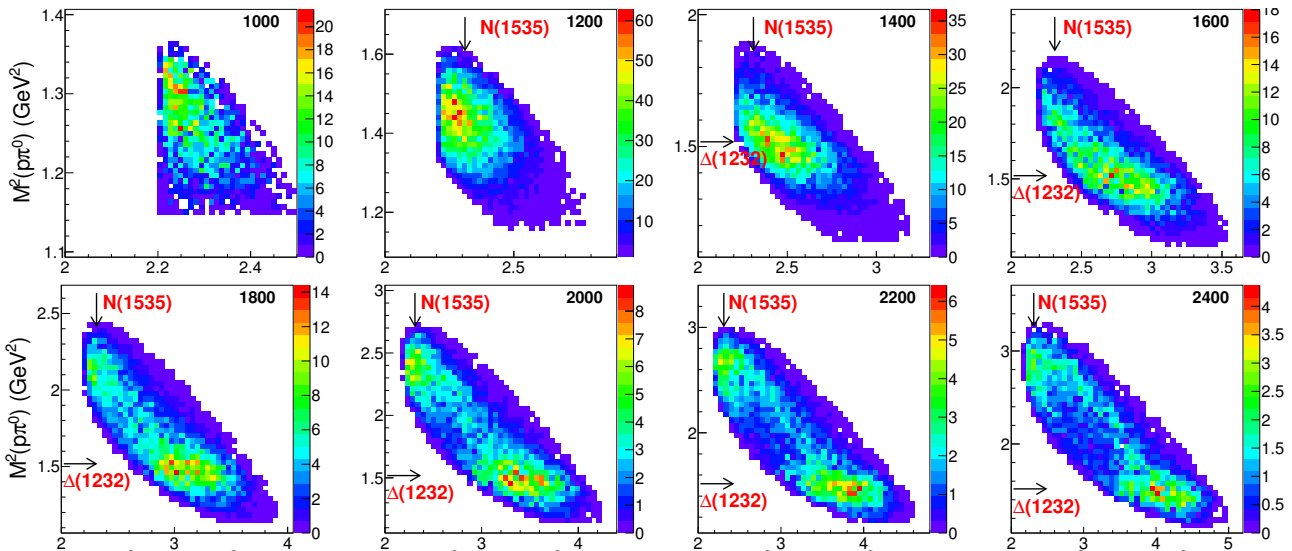


Fig. 20. Dalitz plots $M^2(p\pi^0)$ versus $M^2(p\eta)$ for the incoming photon energy ranges 1000 ± 100 MeV to 2400 ± 100 MeV.

GRAAL and MAMI measurements. We checked all ingredients entering the normalization very carefully, and did not find any reason for this discrepancy. However, the systematic error given in the latter two experiments is much smaller than our estimated error, hence we decided to normalize our cross section using one scaling factor of 0.85 which is applied to the photon flux in the full energy range. This factor is applied in Fig. 19, in all subsequent figures, and in the partial wave analysis. The error which originates from this uncertainty for the decay branching ratios is covered by the systematic error.

In the figure, we also show important isobar contributions as derived in the partial wave analysis described below. The strongest isobar $\Delta(1232)\eta$ defines up to 70% of the total cross section. $N(1535)\pi$ and $p a_0(980)$ provide a significant contribution as well.

6.2 Dalitz plots

Figs. 20-22 show three variants of Dalitz plots for the reaction $\gamma p \rightarrow p\pi^0\eta$ for 100 MeV wide bins in incoming photon energy. Clear structures can be observed in all three squared invariant masses. In Fig. 20, $M^2(p\pi^0)$ is

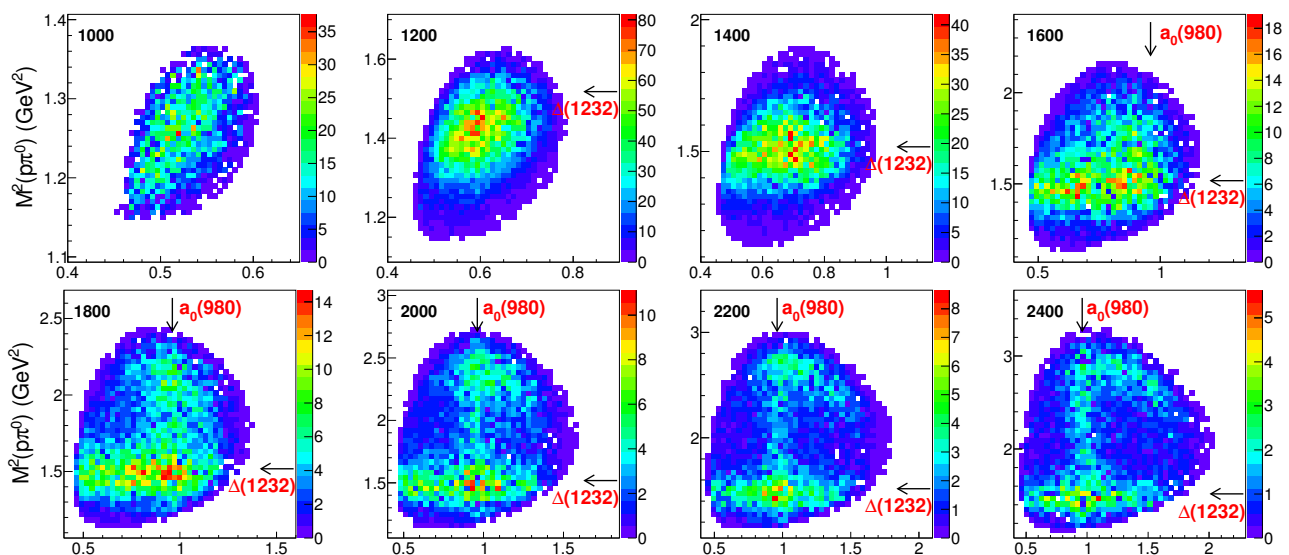


Fig. 21. Dalitz plots $M^2(p\pi^0)$ versus $M^2(\pi^0\eta)$ for the incoming photon energy ranges 1000 ± 100 MeV to 2400 ± 100 MeV.

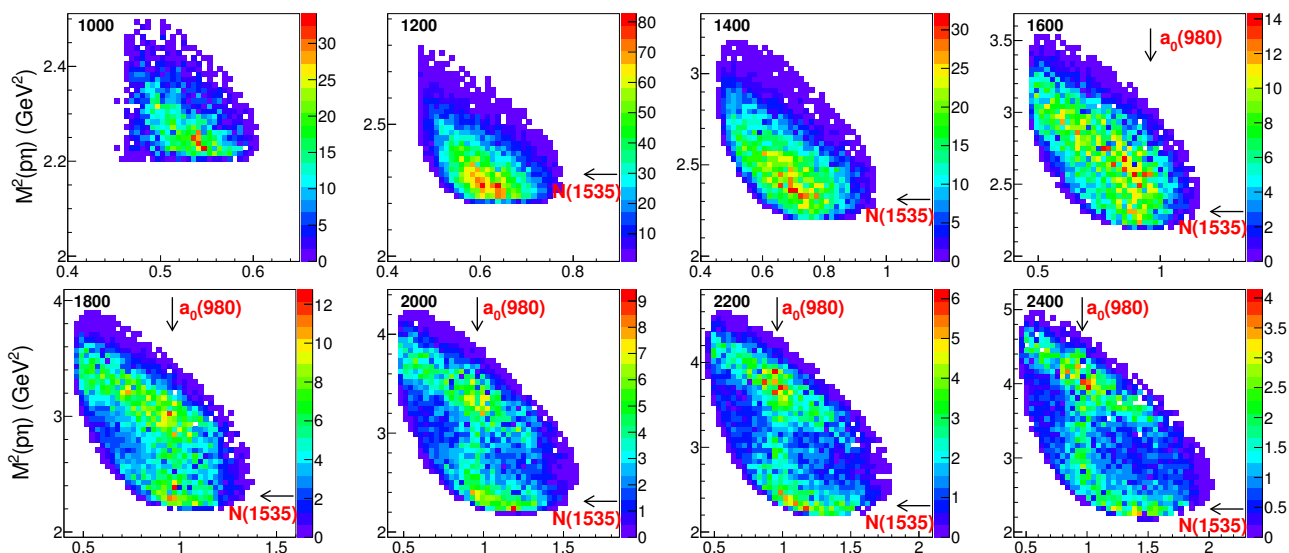


Fig. 22. Dalitz plots $M^2(p\eta)$ versus $M^2(\pi^0\eta)$ for the incoming photon energy ranges 1000 ± 100 MeV to 2400 ± 100 MeV.

shown versus $M^2(p\eta)$. At low energy, an enhancement is observed which develops into two separate active areas when higher energies are reached. The two areas can be identified with the production of $N(1535)\pi$, with $N(1535)$ decaying into $p\eta$, and of $\Delta(1232)\eta$, with Δ decaying into $p\pi^0$. In the second diagonal, a faint band corresponding to the production of $a_0(980)$ mesons recoiling against a proton. The $a_0(980)$ meson is directly visible as a vertical band in Fig. 21 and Fig. 22. The former figure shows again clear evidence for $\Delta(1232)\eta$ production, the latter one for $N(1535)\pi$. The highest intensity is observed at the crossings of the two bands. Evidently, interference will be important in the partial wave analysis. These are particularly sensitive to the phases of the amplitudes and help identify resonant behavior. The findings observed in

the visual inspection of the Dalitz plots are confirmed in the mass distributions given below.

6.3 Mass distributions

Figs. 23 and 24 show mass distributions (in μb per mass bin) for 100 MeV wide bins in the photon energy. From a summation over all mass bins in a photon energy bin, the total cross section can be recalculated. At a photon energy of 1650 MeV, $\Delta(1232)$ production becomes visible above a smooth background, see Fig. 23 (left). $\Delta(1232)$ production becomes increasingly important and continues to make a significant contribution to the cross section up to the highest energies. In Fig. 23 (right) an identifiable threshold enhancement becomes visible at about 1700 MeV photon

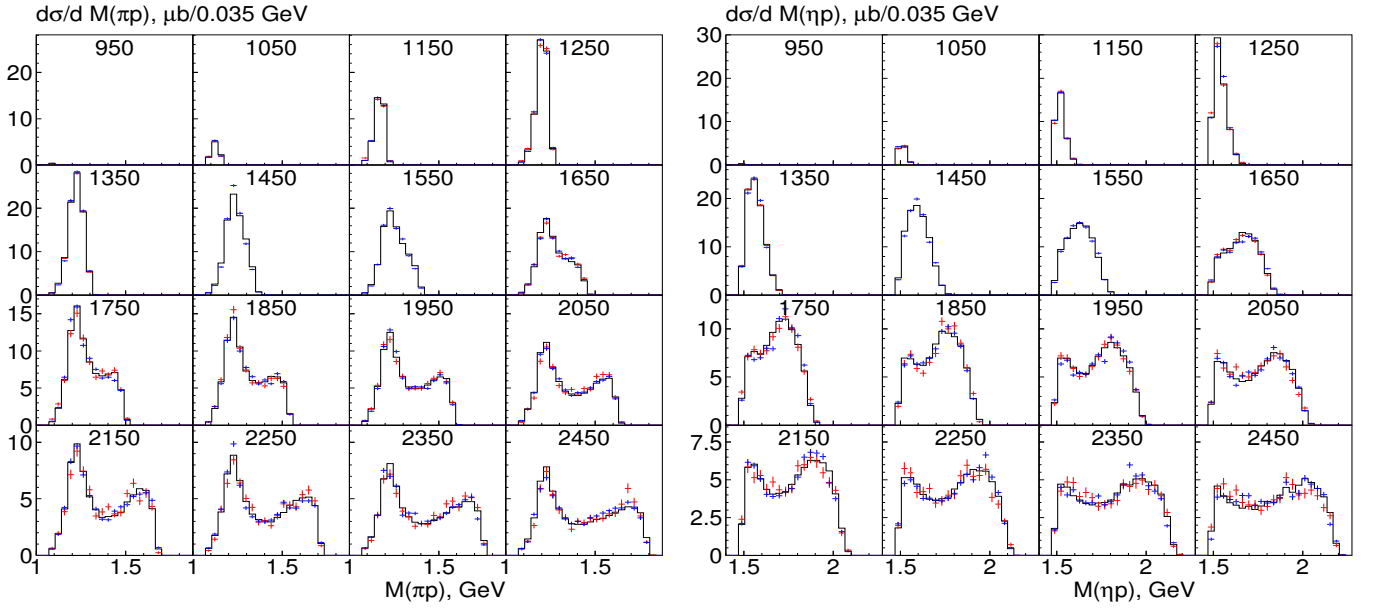


Fig. 23. Differential cross sections $d\sigma/dM_{\pi^0 p}$ (left) and $d\sigma/dM_{\eta p}$ (right). Red points: CB/TAPS1, blue points: CB/TAPS2, histogram: BnGa2013 PWA fit. Numbers denote the center of 100 MeV wide bins in incoming photon energy.

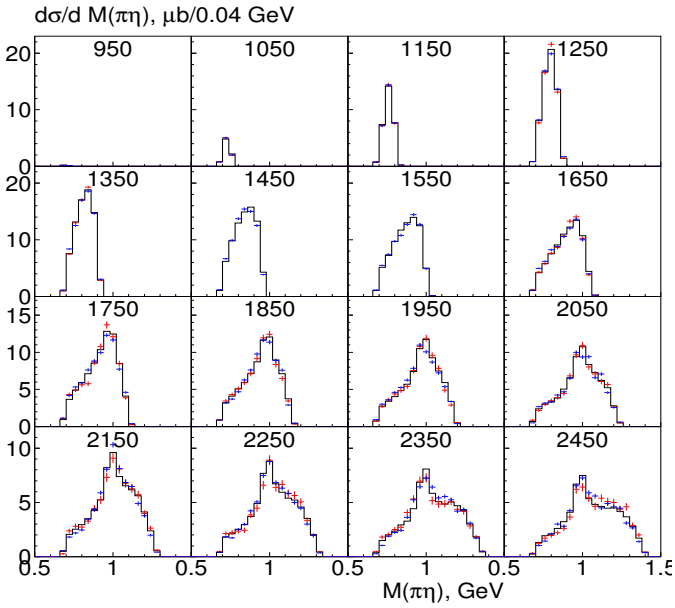


Fig. 24. Differential cross sections $d\sigma/dM_{\pi^0\eta}$. See Fig. 23 for further explanations.

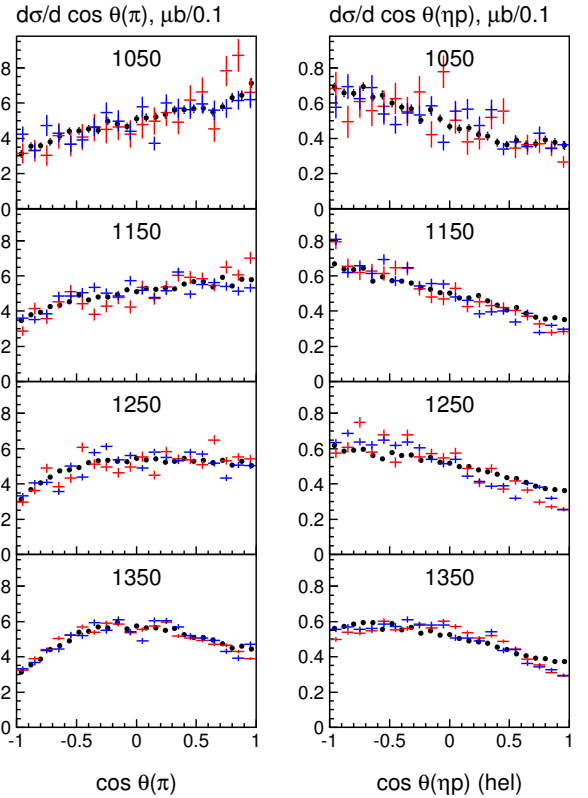


Fig. 25. Comparison of CBELSA/TAPS (red/blue) and MAMI (black) Differential cross-sections in the cm (left) and helicity (right) systems. Numbers denote the center of 100 MeV wide bins in incoming photon energy.

energy; the clearest evidence for $N(1535)$ production is seen at around 2150 MeV. Fig. 24 exhibits a narrow peak at ≈ 980 MeV which we identify with $a_0(980)$. Its contribution to the cross section rises slowly with photon energy and reaches a plateau at about 2000 MeV.

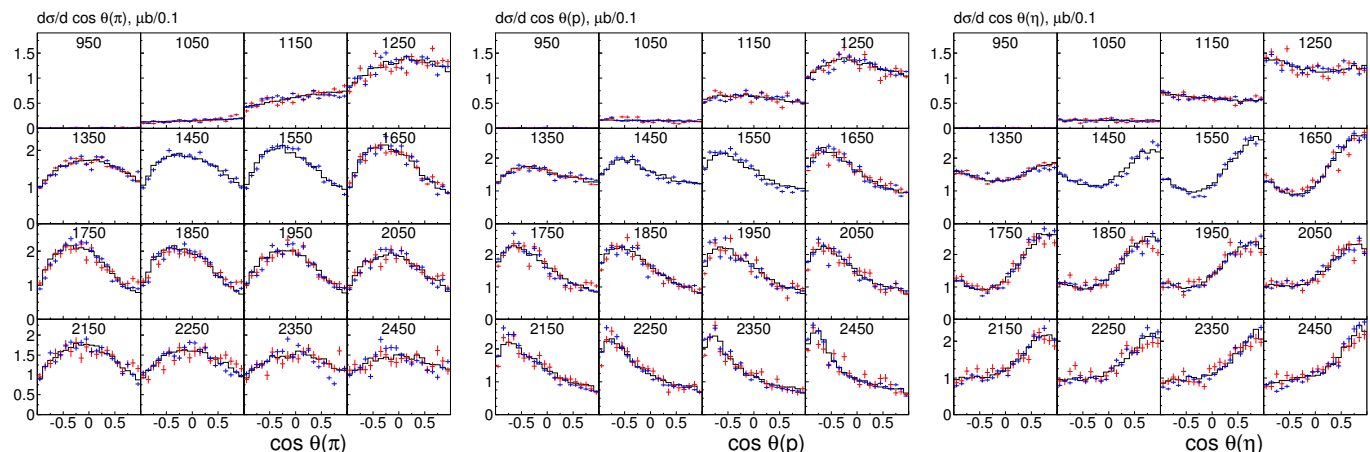


Fig. 26. Differential cross-sections in the center-of-mass system. $d\sigma/d(\cos \pi)$ (left), $d\sigma/d(\cos p)$ (center), $d\sigma/d(\cos \eta)$ (right.) Red points: CB/TAPS1, blue points: CB/TAPS2, histogram: BnGa2013 PWA fit. Numbers denote the center of 100 MeV wide bins in incoming photon energy.

6.4 Comparison with other data

In Fig. 25 our differential distributions are compared with those measured at MAMI [47]. The MAMI data have a significant better statistics but are limited in energy. The agreement between both measurements is very good, suggesting that the acceptance is well understood in both experiments.

6.5 Angular distributions

The 3-body final state in the reaction $\gamma p \rightarrow p\pi^0\eta$ can be characterized by several angular distributions. The $\pi^0\eta$ subsystem can be treated as an ordinary meson (and contains at least the scalar $a_0(980)$ meson) and can be used to define differential cross-sections in the center-of-mass system. In Fig. 26, this differential cross-section is given as a function of the cosine of the scattering angle of the recoiling proton, $\cos \theta_p$. Similarly, $\cos \theta_\pi$ gives the differential cross-section of the π^0 recoiling against the $p\eta$ subsystem, and $\cos \theta_\eta$ for the η recoiling against $p\pi^0$. With a mass cut on $\Delta(1232)$ (and background subtraction), $d\sigma/\cos \theta_\eta$ would be the cross-section for the reaction $\gamma p \rightarrow \Delta(1232)\eta$.

Two additional angular distributions are often shown which are defined in the rest frame of a two-particle subsystem, (e.g., of the $\pi\eta$ subsystem). In both systems, the y -axis is defined by the reaction-plane normal and the x - and z -axis lie in the reaction plane. In the helicity frame (HEL), the z -axis is taken in the direction of the outgoing two-particle system (e.g. $\pi\eta$), while in the Gottfried-Jackson frame GJ the z -axis is taken along the incoming photon. The distributions are shown in Fig. 27 and 28.

6.6 Polarization observables

A subset of the data presented above has been taken with a linearly polarized photon-beam and an unpolarized target.

It was analyzed with respect to polarization observables. Prior to our earlier analysis [49], two-meson production has been treated in a quasi two-body approach [46, 67], resulting in the extraction of the beam asymmetry Σ , known from single-meson photoproduction. The beam asymmetries Σ accessible in $\pi^0\eta$ photoproduction are presented in the next paragraphs. However, a three-body final state like $p\pi^0\eta$ yields additional degrees of freedom, reflected in a different set of polarization observables [48]. These will be discussed in detail in the last part of this section.

Quasi two-body approach In a first approach, one can apply the well-known techniques from single-meson production to extract polarization observables for two-meson final states. For the $p\pi^0\eta$ final state this translates to the three quasi two-body reactions:

$$\begin{aligned} \gamma p &\rightarrow pX, \quad \text{with } X \rightarrow \pi^0\eta, \\ \gamma p &\rightarrow \eta Y, \quad \text{with } Y \rightarrow p\pi^0, \\ \gamma p &\rightarrow \pi^0 Z, \quad \text{with } Z \rightarrow p\eta. \end{aligned}$$

The cross-section for such two-body final states can be written as [68]

$$\frac{d\sigma}{d\Omega} = \left(\frac{d\sigma}{d\Omega} \right)_0 (1 + \delta_l \Sigma \cos 2\phi), \quad (19)$$

where $\left(\frac{d\sigma}{d\Omega} \right)_0$ is the unpolarized cross-section and δ_l the degree of linear polarization (see Fig. 14). In this work, the angle ϕ is defined as depicted in Fig. 29 (left). The beam asymmetry Σ can then be extracted from the amplitude of the $\cos 2\phi$ modulation of the ϕ -distributions of the individual final state particles. An example is shown in Fig. 30, left. Here, the ϕ -distribution of the final state π^0 has been fitted, according to eq. (19), with the expression

$$f(\phi) = A + P \cdot B \cdot \cos 2\phi, \quad (20)$$

where the degree of linear polarization, P , has been determined event by event and was later averaged for each

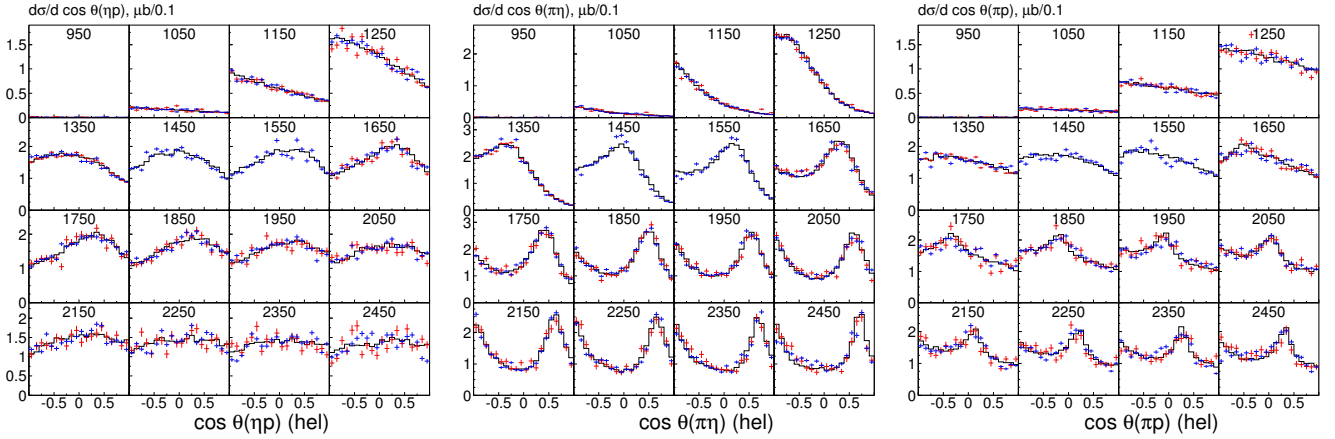


Fig. 27. Differential cross-sections $d\sigma/d\Omega$ in the helicity frame. See Fig. 26 for further explanations.

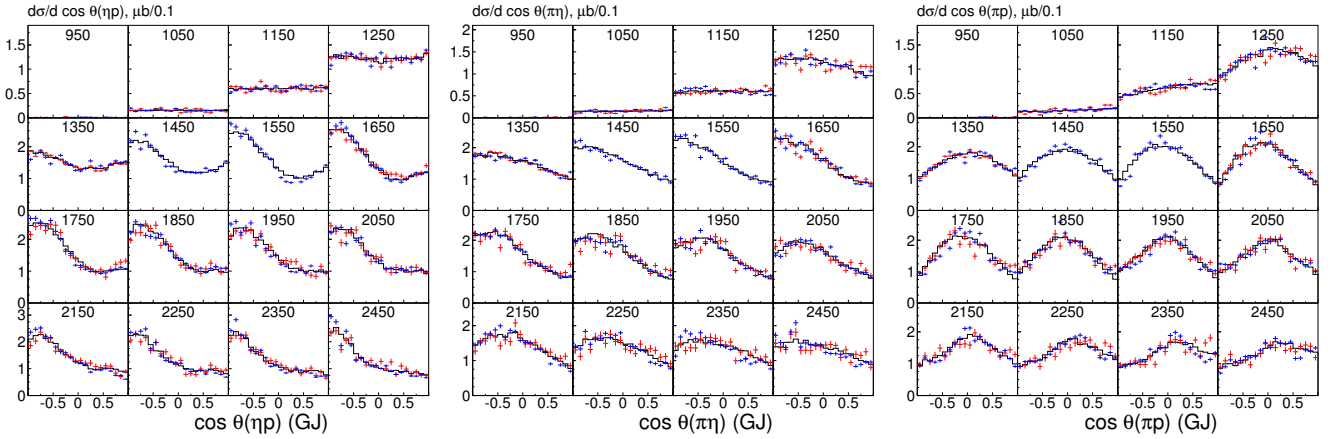


Fig. 28. Differential cross-sections $d\sigma/d\Omega$ in the Gottfried-Jackson frame. See Fig. 26 for further explanations.

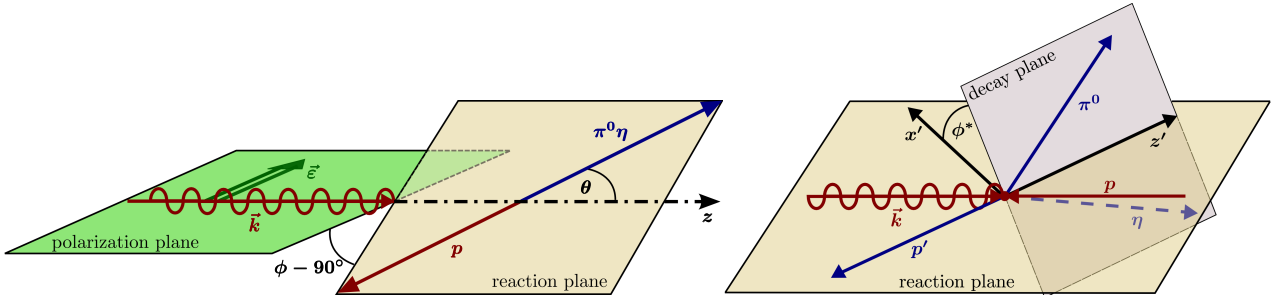


Fig. 29. Angle definitions for the extraction of beam asymmetries. Left: Quasi two-body approach. Right: Additional degree of freedom occurring in full three-body kinematics.

fitted bin. In this ansatz, the ratio of the parameter B/A translates to the beam asymmetry Σ .

The values for the observable are shown in Fig. 31 for the three energy ranges under consideration and extracted from the ϕ -distributions of all three final-state particles, as function of the invariant masses of the respective other two particles (left) and of the $\cos\theta$ of the recoiling particle itself (right).

Using bin sizes in the 5-dimensional phase space sufficiently small compared to variations of the acceptance, the asymmetries should not be influenced by these factors

since they cancel out. However, due to geometrical limitations present in every experimental setup, the phase space is not covered completely, leading to areas of vanishing acceptance. Two different methods have been applied to the data to estimate the influence of acceptance variations and other systematic effects on the results. In a first step, the two-dimensional acceptance has been determined from Monte Carlo simulations for the three energy ranges separately as function of ϕ of the recoiling particle and the variable intended for binning the polarization observable. The data have been corrected for this acceptance, determin-

ing the resulting change in the observables for each bin. In a second step, the Bonn-Gatchina partial wave analysis (BnGa-PWA, described below) has been used to determine the five-dimensional acceptance for the reaction, accounting also for the contributing physics amplitudes. Again, the differences in terms of the beam asymmetry in the relevant binning have been calculated using this correction. The larger absolute value derived from these methods is given in Fig. 31 as grey bars, corresponding to an estimate of the systematic error.

Full three-body approach The cross-section for the production of pseudoscalar meson pairs can be written in the form

$$\frac{d\sigma}{d\Omega} = \left(\frac{d\sigma}{d\Omega} \right)_0 (1 + \delta_l (I^c(\phi^*) \cos 2\phi + I^s(\phi^*) \sin 2\phi)). \quad (21)$$

The two polarization observables I^s and I^c emerge as the amplitudes of the respective modulations of the azimuthal distributions of the final state particles (Fig. 30, right), once the acoplanar kinematics of the reaction are taken into account (Fig. 29, right). The angular dependence of the observables

$$I^s(\phi^*) = \sum_{n=0} a_n \sin(n\phi^*) \rightarrow I^s(\phi^*) = -I^s(2\pi - \phi^*) \quad (22)$$

and

$$I^c(\phi^*) = \sum_{n=0} b_n \cos(n\phi^*) \rightarrow I^c(\phi^*) = I^c(2\pi - \phi^*) \quad (23)$$

allows for a direct cross-check of the data with respect to systematic effects [49]. Additionally it is to be noted that the two-body beam asymmetry Σ occurs here as the constant term in the expansion of I^c .

Fig. 32 shows the obtained beam asymmetries as function of the angle ϕ^* (solid symbols) for the three photon-energy ranges 970-1200 MeV, 1200-1450 MeV and 1450-1650 MeV, along with the data after application of transformations (22), (23) (open symbols). In the absence of systematic effects, both sets of data should coincide. Taking into account the statistical uncertainties, this is well fulfilled, proving the quality of the data.

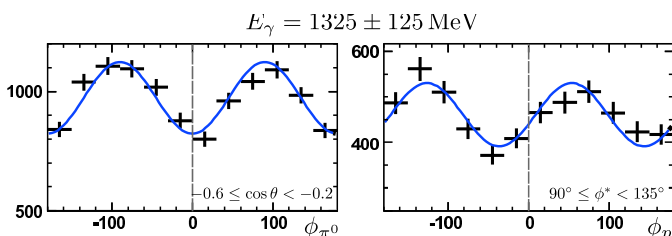


Fig. 30. Left: ϕ -distribution of the final state π^0 in a quasi two-body approach, binned in $\cos \theta_\pi$. Only the $\cos 2\phi$ -modulation according to eq. (19) is visible. Right: ϕ -distribution of the final state p in a full three-body approach, binned in ϕ^* . An additional $\sin 2\phi$ -modulation, according to eq. (21) is apparent.

The comparison of the theoretical approaches used for the interpretation of the data on the beam asymmetries shows the complexity of the reaction $\gamma p \rightarrow p\pi^0\eta$, once the incoming photon energy sufficiently exceeds the threshold energy for the process. A good description at low energies is already achieved by including just one resonant process, the excitation of the $\Delta(1700)3/2^-$, dominating the threshold region, as first introduced by the Valencia group in [51]. The results are also consistent with the assumption that this resonance is in fact dynamically generated by meson-baryon interactions [50]. The continued dominance of the partial wave with $(I)J^P = (3/2)3/2^-$, at higher energies populated by the $\Delta(1940)3/2^-$, first claimed by the BnGa-PWA group in [38], is confirmed by the Fix-model [69]. Figs. 31 and 32 compare our data with the fits from [50,69] and the BnGa2013 fit.

7 Partial wave analysis

7.1 Aims

The partial wave analysis serves two purposes: it is required to determine the acceptance and to extract the physical content of the data. The use of the partial wave analysis for the acceptance correction can best be understood in the case of a simple spectrum like the angular distribution in $\cos \theta$. Often, the full angular range is not covered experimentally, hence the distribution has to be extrapolated into regions with no data. This can be done using a polynomial extrapolation but, of course, an extrapolation with a partial wave analysis is better. In the case of a three-body final state, there are five independent variables, the photon energy and, e.g., two invariant masses used to construct a Dalitz plot, and two Euler angles describing the orientation of the Dalitz plot relative to the direction of the incoming beam. Hence an extrapolation into the four-dimensional phase space (for each bin in E_γ) is required; this is not possible using a polynomial expansion.

The second (and main) purpose of the partial wave analysis is to determine properties of baryon resonances. In the presentation of the data, evidence was seen for $\Delta(1232)\pi$, $N(1535)1/2^- \pi$, and $pa_0(980)$ as intermediate isobars. There are immediate questions: how are they produced? Via u - or t -channel exchange processes, as direct three-body production, or via resonance formation and a subsequent cascade decay? If the latter is the case, which primary resonances contribute? Are there new resonances, so far *missing resonances* involved? Can further intermediate isobars be identified?

Dynamical coupled-channels models based on effective chiral Lagrangians provide a microscopical description of the background [70,71]. In some cases, resonances can even be constructed from the iteration of background terms [72,73,74]. We follow a more phenomenological approach based on a K-matrix. The formalism is described in detail in [75,76]. Here we give a short outline, mainly to introduce the definitions of the quantities presented in the tables below.

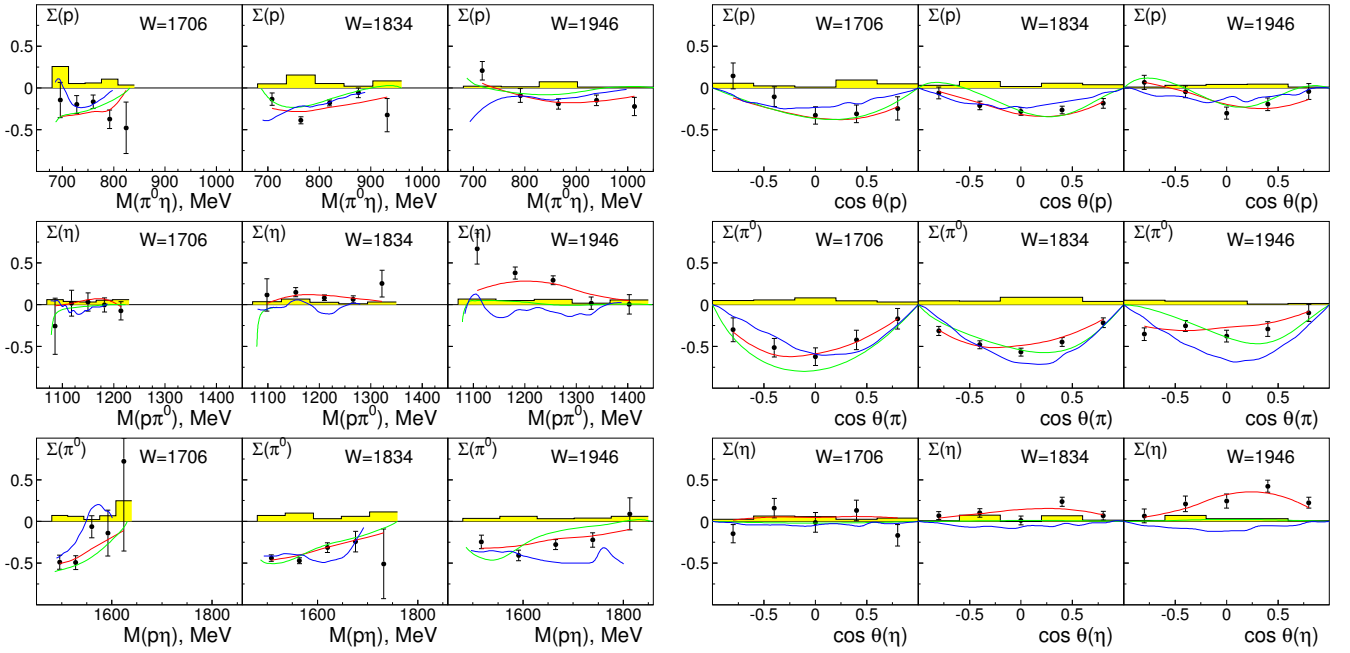


Fig. 31. Two-body beam asymmetry Σ for the reaction $\gamma p \rightarrow p\pi^0\eta$. Top to bottom: incoming photon energy ranges 1085 ± 115 MeV, 1325 ± 125 MeV, 1550 ± 100 MeV. Left: Asymmetries obtained from the ϕ -distributions of the recoiling (left to right) p , η , π^0 as function of the invariant mass of the other two particles [67]. Right: The same as function of the $\cos \theta$ of the recoiling particle. Systematic error estimate from acceptance studies (yellow). Curves: BnGa-PWA (red), Fix et al. [69] (green), Döring et al. [50] (blue).

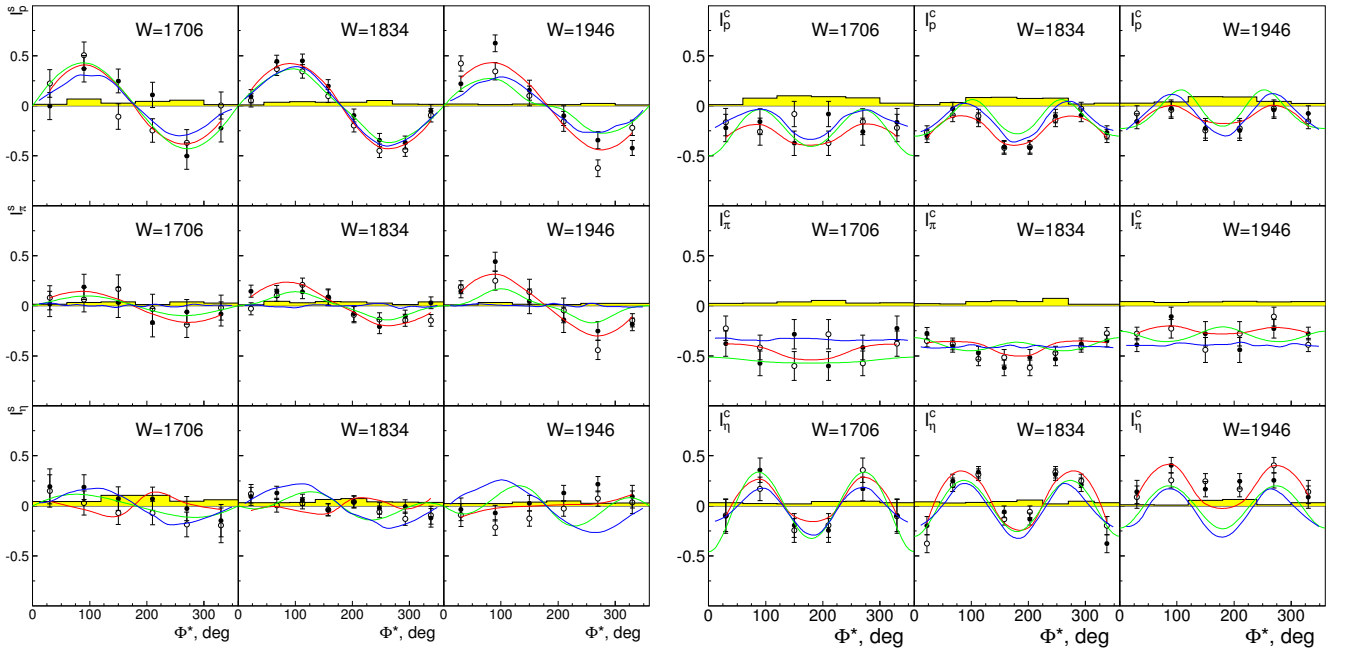


Fig. 32. Three-body beam asymmetries I^s (left) and I^c (right) [49]. Closed symbols: $I^s(\phi^*)$ ($I^c(\phi^*)$) as extracted from the data, open symbols: $(-I^s(2\pi - \phi^*), I^c(2\pi - \phi^*))$ see eqs. (23, 22) Grey bars: Systematic error estimate from acceptance studies. Curves: BnGa-PWA (red), Fix et al. [69] (green), Döring et al. [50] (blue).

7.2 The formalism

The transition amplitude for pion- and photo-produced reactions from an initial state, e.g. $a = \pi N$ or γN , to a

final state, e.g. $b = \Lambda K^+$, can be written in the form of a K-matrix as

$$A_{ab} = K_{ac}(I - i\rho K)_{cb}^{-1}, \quad (24)$$

where ρ is a diagonal matrix of effective phase volumes. For a two body final state the effective phase volume in a partial wave with a relative orbital angular momentum L rises at threshold with q^{2L+1} where q is the decay momentum. To describe the high-energy behavior of the cross-section, form factors are used as suggested by Blatt and Weisskopf [77]:

$$\rho_b(s) = \frac{2q}{\sqrt{s}} \frac{q^{2L}}{F(r^2, q^2, L)}. \quad (25)$$

Here r is an effective interaction radius and the explicit form of the Blatt-Weisskopf form factor can be found in Appendix C of [75]. For three body final states we use the dispersion integral (the explicit form is given in [76]) which takes into account all corresponding threshold singularities on the real axis and in the complex energy plane.

The amplitude contains resonances in the form of K-matrix poles (characterized by the pole position M_α and couplings g_a^α) and non-resonant terms for direct transitions f_{ab} between different channels:

$$K_{ab} = \sum_\alpha \frac{g_a^\alpha g_b^\alpha}{M_\alpha^2 - s} + f_{ab}. \quad (26)$$

The background terms f_{ab} can be arbitrary functions of s . In general we introduce an s -dependence in the form

$$f_{ab} = \frac{(a + b\sqrt{s})}{(s - s_0)}. \quad (27)$$

In most cases, the form (27) did not lead to a noticeable improvement of the fit but sometimes to a poor convergence. For the majority of transitions (for all partial waves with orbital momentum $L > 1$ and for all transitions into three body final states) a constant background term was sufficient to describe the data. In the fits, amplitudes for reggeized exchanges in the t - and u -channel were added.

In practice we neglect in our analysis contributions from γN loop diagrams in rescattering. Thus we do not take into account the γN channel in the K-matrix equation (24) and describe photoproduction of mesons within the P-vector formalism [79]:

$$A_{hb} = P_{hc}(I - i\rho K)_{cb}^{-1}, \quad P_{hc} = K_{hc}, \quad (28)$$

where the h denotes the helicity of the initial state and where b, c list the hadronic final states.

7.3 Particle properties at the pole position

We define the pole position by a zero of the amplitude denominator in the complex plane

$$\prod_\alpha (M_\alpha^2 - s) \det(I - i\rho K) = 0. \quad (29)$$

In the case of a one-pole K-matrix without non-resonant terms (which corresponds to a relativistic Breit-Wigner amplitude) this equation has a simple form:

$$M^2 - s - i \sum_j g_j^2 \rho_j(s) = 0. \quad (30)$$

The residues for the transition amplitude from a to b can be calculated by a contour integral of the amplitude around the pole position in the energy (\sqrt{s}) plane

$$\begin{aligned} Res(a \rightarrow b) &= \int_0 \frac{d\sqrt{s}}{2\pi i} \sqrt{\rho_a} A_{ab}(s) \sqrt{\rho_b} \\ &= \frac{1}{2M_p} \sqrt{\rho_a(M_p^2)} g_a^r g_b^r \sqrt{\rho_b(M_p^2)}. \end{aligned} \quad (31)$$

Here M_p is the position of the pole (complex number) and g_a^r are pole couplings. For elastic scattering of channel a to a , e.g. for $\pi N \rightarrow \pi N$, this gives the elastic residue

$$Res(\pi N \rightarrow N\pi) = \frac{1}{2M_p} (g_{N\pi}^r)^2 \rho_{N\pi}(M_p^2) \quad (32)$$

At the pole position the amplitude factorizes:

$$Res^2(a \rightarrow b) = Res(a \rightarrow a) \times Res(b \rightarrow b). \quad (33)$$

This relation can be used to define branching ratios at the pole position as

$$BR_{\text{pole}}(\text{channel } b) = \frac{|Res(\pi N \rightarrow b)|^2}{|Res(\pi N \rightarrow N\pi)| \cdot (\Gamma_{\text{pole}}/2)}. \quad (34)$$

The helicity amplitudes for photoproduction of the final state b , $\tilde{A}_{1/2}$ and $\tilde{A}_{3/2}$, calculated at the pole position are given by

$$\tilde{A}_h = \sqrt{\frac{\pi(2J+1)m_{\text{pole}}}{k_{\text{pole}}^2 m_N}} \frac{Res(h \rightarrow b)}{\sqrt{Res(b \rightarrow b)}} \quad (35)$$

where the residues (Res) are evaluated at the pole mass (m_{pole}), and $k_{\text{pole}}^2 = (m_{\text{pole}}^2 - m_N^2)^2 / 4m_{\text{pole}}^2$ [80]. The transition amplitude from the fixed helicity is correspondingly defined as

$$(\gamma N)^{h \rightarrow b} = \sqrt{\frac{\pi(2J+1)m_{\text{pole}}}{k_{\text{pole}}^2 m_N}} Res(h \rightarrow b). \quad (36)$$

In the Tables below, we give multipole transition amplitudes $E_{L\pm}$ and $M_{L\pm}$ for production and decay of resonances. The multipoles can be expressed in terms of the helicity amplitudes. For states with $J = L+1/2$:

$$\begin{aligned} \tilde{E}_{L+} &= \frac{-1}{L+1} \left(\tilde{A}_{1/2} - \tilde{A}_{3/2} \sqrt{\frac{L}{L+2}} \right) & L \geq 0, \\ \tilde{M}_{L+} &= \frac{-1}{L+1} \left(\tilde{A}_{1/2} + \tilde{A}_{3/2} \sqrt{\frac{L+2}{L}} \right) & L \geq 1, \end{aligned} \quad (37)$$

where J is the total momentum, L is the orbital momentum in the πN channel. For states with $J = L-1/2$:

$$\begin{aligned} \tilde{E}_{L-} &= \frac{-1}{L} \left(\tilde{A}_{1/2} + \tilde{A}_{3/2} \sqrt{\frac{L+1}{L-1}} \right) & L \geq 2, \\ \tilde{M}_{L-} &= \frac{1}{L} \left(\tilde{A}_{1/2} - \tilde{A}_{3/2} \sqrt{\frac{L-1}{L+1}} \right) & L \geq 1, \end{aligned} \quad (38)$$

In Table 4 below, the helicity and electric and magnetic transition amplitudes at the pole position are abbreviated as $(\gamma p)^h \rightarrow b$, $(\gamma p \rightarrow b; E_{L\pm})$, and $(\gamma p \rightarrow b; M_{L\pm})$, respectively.

7.4 Particle properties from Breit-Wigner representations

A K-matrix fit returns an amplitude with poles in the complex plane, Breit-Wigner parameters do not result from those fits. Here, the Breit-Wigner parameters are calculated from the pole position of the resonance. The procedure is described in [32]. We shortly review it for convenience of the reader. We define a Breit-Wigner amplitude as

$$A_{ab} = \frac{f^2 g_a^r g_b^r}{M_{BW}^2 - s - if^2 \sum_a |g_a^r|^2 \rho_a(s)} \quad (39)$$

where g_a^r are coupling residues at the pole, M_{BW} is the Breit-Wigner mass and f is a scaling factor. The Breit-Wigner mass and scaling factor are adjusted to reproduce the pole position of the resonance. In the case of very fast growing phase volumes, the Breit-Wigner mass and width can shift from the pole position by a large amount. In the 1600-1700 MeV region, the large phase volume leads to a very large Breit-Wigner width and an appreciable shift in mass from the pole position (see for example [81]). The visible width, e.g. in the $N\pi$ invariant mass spectrum, remains similar to the Breit-Wigner width. The large phase volume effects are highly model dependent. We therefore extract the Breit-Wigner parameters of resonances above the Roper resonance by approximating the phase volumes for the three body channels in eq. (39) as πN phase volume for the respective partial wave. This procedure conserves the branching ratio between three-particle final states and the πN channel at the resonance position.

The Breit-Wigner helicity amplitude is defined as

$$(\gamma N)^h \rightarrow b = \frac{A_{BW}^h f g_b^r}{M_{BW}^2 - s - if^2 \sum_a |g_a^r|^2 \rho_a(s)}, \quad (40)$$

where A_{BW}^h is calculated to reproduce the pion photoproduction residues in the pole. In general, this quantity is a complex number. However, for the majority of resonances its phase deviates not significantly from 0 or 180 degrees and the sign can be defined as sign of the real part. $A_{1/2}$ and $A_{3/2}$ are normalized to satisfy

$$\Gamma_\gamma = \frac{k_{BW}^2}{\pi} \frac{2m_N}{(2J+1)m_{BW}} \left(|A_{1/2}|^2 + |A_{3/2}|^2 \right) \quad (41)$$

when the pole position is replaced by the Breit-Wigner mass.

For Breit-Wigner amplitudes, $m_{\text{pole}} = m_{BW}$ and $\tilde{A}_h = A_h$.

Table 2. Change in χ^2 of the multichannel fit when the coupling of a resonance to different decay modes is set to zero and the data refitted. If contributions are found to be very small, they are set to zero (to improve the fit stability). In this case, a - is given. Mesonic t -channel exchange is represented by reggeized ρ/ω -exchange, u -channel exchange by proton and Δ exchange.

	$\Delta(1232)\eta$	$N(1535)1/2^-\pi$	$p a_0(980)$
$N(1710)1/2^+$	-	656	-
$N(1880)1/2^+$	-	23	166
$N(1900)3/2^+$	-	883	108
$N(2100)1/2^+$	-	323	156
$N(2120)3/2^-$	-	169	-
$\Delta(1700)3/2^-$	1333	263	-
$\Delta(1900)1/2^-$	198	-	-
$\Delta(1905)5/2^+$	328	337	-
$\Delta(1910)1/2^+$	1195	-	-
$\Delta(1920)3/2^+$	273	-	204
$\Delta(1940)3/2^-$	1545	162	-
$\Delta(1950)7/2^+$	476	-	-
ρ/ω exchange	849	-	696
p exchange	299	-	189

7.5 t - and u -channel exchange amplitudes

The amplitudes for t -channel meson exchange in photoproduction are described by reggeized trajectories:

$$A = g_1(t)g_2(t) \frac{1 + \xi \exp(-i\pi\alpha(t))}{\sin(\pi\alpha(t))} \left(\frac{\nu}{\nu_0} \right)^{\alpha(t)}, \quad (42)$$

where $\nu = \frac{1}{2}(s - u)$, $\alpha(t)$ is the function which describes the trajectory, ν_0 is a normalization factor and ξ is the signature of the trajectory. In the case of $\pi^0\eta$ photoproduction, both ρ and ω exchanges (which have positive signature $\xi = +1$) can contribute to the fit. We do not introduce these exchanges separately using an “effective” ρ meson exchange. The structure of the upper and lower vertices is given in detail in [75]. The upper and lower vertices are parameterized with a form factor proportional to $\exp(-\beta t)$, where β is a fit parameter.

The contributions from u -channel (proton) exchange are described by a proton exchange amplitude which contains a proton propagator in the u -channel and form factors at the vertices. The t - and u -channel exchanges are introduced for the $\Delta(1232)\eta$ and $a_0(980)p$ final states. For production of $N(1535)1/2^+\pi$ we found very small contributions from t - and u -exchanges; hence they were neglected in the final fit.

7.6 Method

The new data on $\gamma p \rightarrow p\pi^0\eta$, and the accompanying data on $\gamma p \rightarrow p2\pi^0$, have been included in the large data set used in the Bonn-Gatchina (BnGa) multichannel partial wave analysis. The fitted data set contains results on πN elastic and inelastic ($\pi N \rightarrow N\eta, \Lambda K, \Sigma K$) reactions and the very precise data from photoproduction off protons, including information from polarization and double-polarization experiments. A list of data, including references, is given elsewhere [82, 83]; the list is updated in [32] and [84]. The partial wave analysis method used in this analysis is described in detail in [75, 76]. Further information is given in [82].

The fit minimizes the total log likelihood defined by

$$-\ln \mathcal{L}_{\text{tot}} = \left(\frac{1}{2} \sum w_i \chi_i^2 - \sum w_i \ln \mathcal{L}_i \right) \frac{\sum N_i}{\sum w_i N_i} \quad (43)$$

where the summation over binned data contributes to the χ^2 while unbinned data contribute to the likelihoods \mathcal{L}_i . The data presented in this paper, and other data with three particles in the final state, are fitted using an event-based maximum likelihood method which takes all correlations between mass and angular distributions into account. Differences in fit quality are given as χ^2 difference, $\Delta\chi^2 = -2\Delta\mathcal{L}_{\text{tot}}$. For new data, the weight is increased from $w_i = 1$ until a visually acceptable fit is reached. Without weights, low-statistics data e.g. on polarization variables may be reproduced unsatisfactorily without significant deterioration of the total \mathcal{L}_{tot} . The total χ^2 is normalized to avoid an artificial increase in statistics. The χ^2 values per data point are typically between 1 and 2 even though some data give a larger value.

7.7 Significance

The partial wave analysis requires a large number of resonances in the intermediate state. In Table 2, a list of resonances is given which are presently used in the analysis. Also given is the statistical significance (as change in χ^2) when a particular decay mode is removed from the fit and the data refitted.

The strongest contributions come from the $\Delta(1232)\eta$ isobar with $\Delta(1232)$ and η in a relative S -wave, that is from the $(I, J^P) = (3/2, 3/2^-)$ -wave. Strong couplings to $\Delta(1232)\eta$ are known for the $\Delta(1700)3/2^-$ [38, 39, 69], and also $\Delta(1940)3/2^-$ is known to make a significant contribution to reaction (1) [38, 39]. A further resonance with these quantum numbers seems to be required above 2 GeV; it improves the fit but no clear minimum is found in a mass scan. Tentatively, we call it $\Delta(2200)3/2^-$.

We believe decay modes leading to a χ^2 change of more than 1000 to be rather certain (***) , the evidence for decay modes with a $\delta\chi^2 \geq 500$ is estimated to be fair (**), and those with $\delta\chi^2 \geq 200$ to be poor (*).

It has been mentioned that a high significance is not necessarily connected with a large branching ratio for the decay of a particular resonance. The significance can be

Table 3. Branching ratios of nucleon and Δ resonances

Resonance	πN	$N(1535)\pi$	$\Delta(1232)\eta$
$N(1710)1/2^+$	$5\pm 3\%$	$15\pm 6\%$	-
$N(1880)1/2^+$	$6\pm 3\%$	$8\pm 4\%$	-
$N(1900)3/2^+$	$3\pm 3\%$	$7\pm 3\%$	-
$N(2100)1/2^+$	$3\pm 2\%$	$22\pm 8\%$	-
$N(2120)3/2^-$	$5\pm 3\%$	$15\pm 8\%$	-
$\Delta(1700)3/2^-$	$22\pm 4\%$	$1\pm 0.5\%$	$5\pm 2\%$
$\Delta(1900)1/2^-$	$7\pm 2\%$	-	$1\pm 1\%$
$\Delta(1905)5/2^+$	$13\pm 2\%$	$\leq 1\%$	$4\pm 2\%$
$\Delta(1910)1/2^+$	$12\pm 3\%$	$5\pm 3\%$	$9\pm 4\%$
$\Delta(1920)3/2^+$	$8\pm 4\%$	$\leq 2\%$	$11\pm 6\%$
$\Delta(1940)3/2^-$	$2\pm 1\%$	$8\pm 6\%$	$10\pm 6\%$
$\Delta(1950)7/2^+$	$46\pm 2\%$		$\leq 1\%$

poor even in the case of a resonance with a sizable branching ratio into a final state, e.g. $N(1535)1/2^-\pi$, when the resulting pattern in the final state can be described easily by the sum of two other resonances decaying into the same final state.

At its nominal mass, $\Delta(1600)3/2^+$ cannot contribute to the three decay modes listed in Table 2. $\Delta(1600)3/2^+$ is, however, a wide resonance and it may contribute to these decays via its tail. Mathematically, this is treated by an continuation of the decay momentum (which enters, e.g., in the energy-dependent width of the denominator of a Breit-Wigner amplitude)

$$q = \{(M^2 - (m_1 + m_2)^2)(M^2 - (m_1 - m_2)^2)\}^{1/2}/2M \quad (44)$$

into the range of imaginary values. Due to this analytic continuation of the amplitude, $\Delta(1600)3/2^+$ contributes significantly to the final states in Table 2. The branching ratios are, however, defined by the coupling constants at the pole position, and hence they vanish.

7.8 Results

Before presenting the full results of this analysis, we discuss a possible interpretation of the branching ratios. It is the first time that cascade processes of high-mass resonances into a resonance with intrinsic orbital angular momentum (here $N(1535)1/2^-$) are studied. The comparison of these decay modes with decays into $N\pi$ should help to identify mechanisms responsible for the decays of N and Δ resonances.

In Table 3, the branching ratios for decays into $N\pi$, $N(1535)\pi$, and $\Delta(1232)\eta$ are listed while table 4 collects the full information on decay modes of nucleon and $\Delta(1232)$ resonances into $\Delta(1232)\eta$ (for Δ resonances only), into $N(1535)1/2^-\pi$, and into $pa_0(980)$. The values are the central values derived from 12 representative fits to the data.

Table 4. Nucleon and Delta resonances and their properties from the BnGa multichannel partial wave analysis of πN elastic scattering data and from pion and photo-induced inelastic reactions. Along with the name of the resonance, the star rating of the Particle Data Group [85] is given. Helicity couplings, abbreviated as $(\gamma p)^h$, are given in $\text{GeV}^{-\frac{1}{2}}$. $\pi N \rightarrow \pi N$ stands for the elastic pole residue, $2(\pi N \rightarrow X)/\Gamma$ for inelastic pole residues. They are normalized by a factor $2/\Gamma$ with $\Gamma = \Gamma_{\text{pole}}$. For $N(1880)1/2^+$ we find two solutions with distinct photocouplings. Both are given below.

$N(1710)1/2^+$	***	$N(1900)3/2^+$	***
<hr/> <hr/>		<hr/> <hr/>	
$N(1710)1/2^+$ pole parameters		$N(1900)3/2^+$ decay modes	
M_{pole}	1690±15	Γ_{pole}	170±20
$A^{1/2}$	0.052±0.014	Phase:	(-10±50) ^o
$N(1710)1/2^+$ transition residues		$N(1900)3/2^+$ transition residues	
$\pi N \rightarrow \pi N$	6±3 (MeV)	phase	(120±45) ^o
$2(\pi N \rightarrow N(1535)\pi)/\Gamma$	10±4%		(140±40) ^o
$(\gamma p)^{1/2} \rightarrow N(1535)\pi$	M_{1-} 8.5±3.5 10 ⁻³		(25±35) ^o
$N(1710)1/2^+$ Breit-Wigner parameters		$N(1900)3/2^+$ Breit-Wigner parameters	
M_{BW}	1715±20	Γ_{BW}	175±15
Br(πN)	5±3%	Br($N(1535)\pi$)	15±6%
$A_{BW}^{1/2}$	0.050±0.010		
<hr/> <hr/>		<hr/> <hr/>	
$N(1880)1/2^+$	**	$N(2120)3/2^-$	**
<hr/> <hr/>		<hr/> <hr/>	
$N(1880)1/2^+$ decay modes		$N(2120)3/2^-$ decay modes	
M_{pole}	1870±40	Γ_{pole}	220±50
$A^{1/2(1)}$	0.010±0.05	Phase	-(170±40) ^o
$A^{1/2(2)}$	0.038±0.15	Phase	(80±40) ^o
$N(1880)1/2^+$ transition residues		$N(2120)3/2^-$ transition residues	
$\pi N \rightarrow \pi N$	6±4 (MeV)	phase	(70±60) ^o
$2(\pi N \rightarrow N(1535)\pi)/\Gamma$	9±5%		(130±60) ^o
$2(\pi N \rightarrow N a_0(980))/\Gamma$	4±3%		(40±65) ^o
$\gamma p^{1/2(1)} \rightarrow N(1535)\pi$	M_{1-} 1±0.5 10 ⁻³		-(30±50) ^o
$\gamma p^{1/2(1)} \rightarrow N a_0(980)$	M_{1-} < 0.5 10 ⁻³		not defined
$\gamma p^{1/2(2)} \rightarrow N(1535)\pi$	M_{1-} 4.5±2.5 10 ⁻³		-(75±60) ^o
$\gamma p^{1/2(2)} \rightarrow N a_0(980)$	M_{1-} 1±0.5 10 ⁻³		-(40±50) ^o
$N(1880)1/2^+$ Breit-Wigner parameters		$N(2120)3/2^-$ Breit-Wigner parameters	
M_{BW}	1875±40	Γ_{BW}	230±50
Br(πN)	6±3%	Br($N(1535)\pi$)	8±4%
Br($N a_0(980)$)	3±2%		
$A_{BW}^{1/2(1)}$	-0.010±0.005	$ A_{BW}^{1/2(2)} $	0.038±0.015
<hr/> <hr/>		<hr/> <hr/>	
$\Delta(1900)1/2^-$	**	$\Delta(1910)1/2^+$	****
<hr/> <hr/>		<hr/> <hr/>	
$\Delta(1900)1/2^-$ decay modes		$\Delta(1910)1/2^+$ decay modes	
M_{pole}	1845±20	Γ_{pole}	295±35
$A^{1/2}$	0.059±0.015	Phase	(60±20) ^o
$\Delta(1900)1/2^-$ transition residues		$\Delta(1910)1/2^+$ transition residues	
$\pi N \rightarrow \pi N$	11±2 (MeV)	phase	-(115±20) ^o
$2(\pi N \rightarrow \Delta(1232)\eta)/\Gamma$	1.3±0.6%		not defined
$(\gamma p)^{1/2} \rightarrow \Delta(1232)\eta E_{0+}$	1.1±0.6 10 ⁻³		-(110±60) ^o
$\Delta(1900)1/2^-$ Breit-Wigner parameters		$\Delta(1910)1/2^+$ Breit-Wigner parameters	
M_{BW}	1840±20	Γ_{BW}	295±30
Br(πN)	7±2%	BR($\Delta(1232)\eta$)	1±1%
$A_{BW}^{1/2}$	0.057±0.014		
<hr/> <hr/>		<hr/> <hr/>	
$\Delta(1900)1/2^-$ decay modes		$\Delta(1910)1/2^+$ decay modes	
M_{pole}	1840±40	Γ_{pole}	370±60
$A^{1/2}$	0.027±0.009	Phase	-(30±60) ^o
$\Delta(1910)1/2^+$ transition residues		$\Delta(1910)1/2^+$ transition residues	
$\pi N \rightarrow \pi N$	25±6 (MeV)	phase	-(155±30) ^o
$2(\pi N \rightarrow \Delta(1232)\eta)/\Gamma$	11±4%		-(150±50) ^o
$(\gamma p)^{1/2} \rightarrow \Delta(1232)\eta M_{1-}$	4±3 10 ⁻³		-(80±??) ^o
$\Delta(1910)1/2^+$ Breit-Wigner parameters		$\Delta(1910)1/2^+$ Breit-Wigner parameters	
M_{BW}	1845±40	Γ_{BW}	360±60
Br(πN)	12±3%	BR($\Delta(1232)\eta$)	9±4%
$A_{BW}^{1/2}$	0.026±0.008		
<hr/> <hr/>		<hr/> <hr/>	

Table 6 continued.

$\Delta(1700)3/2^-$				****	$\Delta(1940)3/2^-$				**
$\Delta(1700)3/2^-$ decay modes					$\Delta(1940)3/2^-$ decay modes				
M_{pole}	1685±10	Γ_{pole}	300±15		M_{pole}	2040±50	Γ_{pole}	450±90	
$A^{1/2}$	0.175±0.020	Phase	(50±10) $^\circ$		$A^{1/2}$	0.170 $^{+0.120}_{-0.080}$	Phase	-(10±30) $^\circ$	
$A^{3/2}$	0.180±0.020	Phase	(45±10) $^\circ$		$A^{3/2}$	0.150±0.080	Phase	-(10±30) $^\circ$	
$\Delta(1700)3/2^-$ transition residues				phase	$\Delta(1940)3/2^-$ transition residues				phase
$\pi N \rightarrow \pi N$		40±6 (MeV)	-(1±10) $^\circ$		$\pi N \rightarrow \pi N$		4±3 (MeV)	-(50±35) $^\circ$	
$2(\pi N \rightarrow \Delta(1232)\eta)/\Gamma$		12±2%	-(60±12) $^\circ$		$2(\pi N \rightarrow \Delta(1232)\eta)/\Gamma$		< 1%	not defined	
$2(\pi N \rightarrow N(1535)\pi)/\Gamma$		3.5±1.5%	-(75±30) $^\circ$		$2(\pi N \rightarrow N(1535)\pi)/\Gamma$		< 3%	not defined	
$(\gamma p)^{1/2} \rightarrow \Delta(1232)\eta$		16±3 10 $^{-3}$	-(10±15) $^\circ$		$(\gamma p)^{1/2} \rightarrow \Delta(1232)\eta$		6.5±3 10 $^{-3}$	-(110±55) $^\circ$	
$(\gamma p)^{3/2} \rightarrow \Delta(1232)\eta$		16±3 10 $^{-3}$	-(10±14) $^\circ$		$(\gamma p)^{3/2} \rightarrow \Delta(1232)\eta$		4±2 10 $^{-3}$	-(110±45) $^\circ$	
$(\gamma p)^{1/2} \rightarrow N(1535)\pi$		4.5±2 10 $^{-3}$	-(25±30) $^\circ$		$(\gamma p)^{1/2} \rightarrow N(1535)\pi$		16±6 10 $^{-3}$	-(30±20) $^\circ$	
$(\gamma p)^{3/2} \rightarrow N(1535)\pi$		4.5±2 10 $^{-3}$	-(30±30) $^\circ$		$(\gamma p)^{3/2} \rightarrow N(1535)\pi$		11±4 10 $^{-3}$	-(30±20) $^\circ$	
$\gamma p \rightarrow \Delta(1232)\eta$	E_{2-}	22±4 10 $^{-3}$	(170±15) $^\circ$		$\gamma p \rightarrow \Delta(1232)\eta$	E_{2-}	6.7±3 10 $^{-3}$	(65±55) $^\circ$	
$\gamma p \rightarrow \Delta(1232)\eta$	M_{2-}	3.5±0.7 10 $^{-3}$	-(5±20) $^\circ$		$\gamma p \rightarrow \Delta(1232)\eta$	M_{2-}	2±1 10 $^{-3}$	-(110±55) $^\circ$	
$\gamma p \rightarrow N(1535)\pi$	E_{2-}	6±3 10 $^{-3}$	(150±30) $^\circ$		$\gamma p \rightarrow N(1535)\pi$	E_{2-}	18±6 10 $^{-3}$	(150±15) $^\circ$	
$\gamma p \rightarrow N(1535)\pi$	M_{2-}	1±0.5 10 $^{-3}$	-(20±35) $^\circ$		$\gamma p \rightarrow N(1535)\pi$	M_{2-}	6±3 10 $^{-3}$	-(30±15) $^\circ$	
$\Delta(1700)3/2^-$ Breit-Wigner parameters					$\Delta(1940)3/2^-$ Breit-Wigner parameters				
M_{BW}	1715±20	Γ_{BW}	300±25		M_{BW}	2050±40	Γ_{BW}	450±70	
Br(πN)	22±4%	BR($\Delta(1232)\eta$)	5±2%		Br(πN)	2±1%	BR($\Delta(1232)\eta$)	10±6%	
Br($N(1535)\pi$)	1±0.5%				Br($N(1535)\pi$)	8±6%			
$A_{BW}^{1/2}$	0.165±0.020	$A_{BW}^{3/2}$	0.170±0.025		$A_{BW}^{1/2}$	0.170 $^{+0.110}_{-0.080}$	$A_{BW}^{3/2}$	0.150±0.080	
$\Delta(1920)3/2^+$				****	$\Delta(1905)5/2^+$				****
$\Delta(1920)3/2^+$ decay modes					$\Delta(1905)5/2^+$ decay modes				
M_{pole}	1875±30	Γ_{pole}	300±40		M_{pole}	1800±6	Γ_{pole}	290±15	
$A^{1/2}$	0.110±0.030	Phase	-(50±20) $^\circ$		$A^{1/2}$	0.025±0.005	Phase	-(28±12) $^\circ$	
$A^{3/2}$	0.100±0.040	Phase	-(180±20) $^\circ$		$A^{3/2}$	-0.050±0.004	Phase	(5±10) $^\circ$	
$\Delta(1920)3/2^+$ transition residues				phase	$\Delta(1905)5/2^+$ transition residues				phase
$\pi N \rightarrow \pi N$		16±6 (MeV)	-(50±25) $^\circ$		$\pi N \rightarrow \pi N$		19±2 (MeV)	-(45±4) $^\circ$	
$2(\pi N \rightarrow \Delta(1232)\eta)/\Gamma$		15±4%	(70±20) $^\circ$		$2(\pi N \rightarrow \Delta(1232)\eta)/\Gamma$		7±2%	(40±20) $^\circ$	
$2(\pi N \rightarrow N(1535)\pi)/\Gamma$		3±2%	(35±45) $^\circ$		$2(\pi N \rightarrow N(1535)\pi)/\Gamma$		2.5±1%	(130±35) $^\circ$	
$2(\pi N \rightarrow Na_0(980))/\Gamma$		3±2%	-(85±45) $^\circ$		$(\gamma p)^{1/2} \rightarrow \Delta(1232)\eta$		1.8±0.4 10 $^{-3}$	(23±20) $^\circ$	
$(\gamma p)^{1/2} \rightarrow \Delta(1232)\eta$		20±7	(55±30) $^\circ$		$(\gamma p)^{3/2} \rightarrow \Delta(1232)\eta$		4.0±1 10 $^{-3}$	-(135±20) $^\circ$	
$(\gamma p)^{3/2} \rightarrow \Delta(1232)\eta$		17±5	-(75±25) $^\circ$		$(\gamma p)^{1/2} \rightarrow N(1535)\pi$		0.6±0.2 10 $^{-3}$	(120±40) $^\circ$	
$(\gamma p)^{1/2} \rightarrow N(1535)\pi$		5±3 10 $^{-3}$	(10±35) $^\circ$		$(\gamma p)^{3/2} \rightarrow N(1535)\pi$		1.3±0.5 10 $^{-3}$	-(40±35) $^\circ$	
$(\gamma p)^{3/2} \rightarrow N(1535)\pi$		4±3 10 $^{-3}$	-(110±40) $^\circ$		$\gamma p \rightarrow \Delta(1232)\eta$	E_{3-}	1.4±0.4 10 $^{-3}$	(60±20) $^\circ$	
$(\gamma p)^{1/2} \rightarrow Na_0(980)$		5±3 10 $^{-3}$	-(100±50) $^\circ$		$\gamma p \rightarrow \Delta(1232)\eta$	M_{3-}	1.5±0.3 10 $^{-3}$	(40±20) $^\circ$	
$(\gamma p)^{3/2} \rightarrow Na_0(980)$		4±2 10 $^{-3}$	(130±50) $^\circ$		$\gamma p \rightarrow N(1535)\pi$	E_{3-}	0.4±0.2 10 $^{-3}$	(150±35) $^\circ$	
$\gamma p \rightarrow \Delta(1232)\eta$	E_{1+}	18±6 10 $^{-3}$	-(100±30) $^\circ$		$\gamma p \rightarrow N(1535)\pi$	M_{3-}	0.5±0.1 10 $^{-3}$	(130±35) $^\circ$	
$\gamma p \rightarrow \Delta(1232)\eta$	M_{1+}	11±5 10 $^{-3}$	(150±30) $^\circ$		$\Delta(1905)5/2^+$ Breit-Wigner parameters				
$\gamma p \rightarrow N(1535)\pi$	E_{1+}	5±3 10 $^{-3}$	-(150±35) $^\circ$		M_{BW}	1856±6	Γ_{BW}	325±15	
$\gamma p \rightarrow N(1535)\pi$	M_{1+}	5±3 10 $^{-3}$	(110±40) $^\circ$		Br(πN)	13±2%	BR($\Delta(1232)\eta$)	4±2%	
$\gamma p \rightarrow Na_0(980)$	E_{1+}	4±2 10 $^{-3}$	(100±50) $^\circ$		Br($N(1535)\pi$)	< 1%			
$\gamma p \rightarrow Na_0(980)$	M_{1+}	4±2 10 $^{-3}$	-(10±50) $^\circ$		$A_{BW}^{1/2}$	0.025±0.005	$A_{BW}^{3/2}$	-0.050±0.005	
$\Delta(1920)3/2^+$ Breit-Wigner parameters					$\Delta(1950)7/2^+$ continued				
M_{BW}	1880±30	Γ_{BW}	300±40		$\Delta(1950)7/2^+$ transition residues				phase
Br(πN)	8±4%	BR($\Delta(1232)\eta$)	11±6%		$\pi N \rightarrow \pi N$		58±2 (MeV)	-(24±3) $^\circ$	
Br($N(1535)\pi$)	< 2%				$2(\pi N \rightarrow \Delta(1232)\eta)/\Gamma$		3.5±0.5%	(90±25) $^\circ$	
$A_{BW}^{1/2}$	0.110±0.030	$A_{BW}^{3/2}$	0.105±0.035		$(\gamma p)^{1/2} \rightarrow \Delta(1232)\eta$		1.1±0.2 10 $^{-3}$	-(80±25) $^\circ$	
$\Delta(1950)7/2^+$				****	$(\gamma p)^{3/2} \rightarrow \Delta(1232)\eta$		1.6±0.3 10 $^{-3}$	-(80±25) $^\circ$	
$\Delta(1950)7/2^+$ decay modes					$\gamma p \rightarrow \Delta(1232)\eta$	E_{3+}	0.04±0.02 10 $^{-3}$	not defined	
M_{pole}	1888±4	Γ_{pole}	245±8		$\gamma p \rightarrow \Delta(1232)\eta$	M_{3+}	0.75±0.07 10 $^{-3}$	(100±25) $^\circ$	
$A^{1/2}$	-0.067±0.004	Phase	-(10±5) $^\circ$		$\Delta(1905)5/2^+$ Breit-Wigner parameters				
$A^{3/2}$	-0.095±0.004	Phase	-(10±5) $^\circ$		M_{BW}	1917±4	Γ_{BW}	251±8	
					Br(πN)	46±2%	BR($\Delta(1232)\eta$)	< 1%	
					$A_{BW}^{1/2}$	-0.067±0.005	$A_{BW}^{3/2}$	-0.094±0.004	

The fits differ in the number of resonances in a given partial wave and in the weight given to individual data sets, see eq. (43). The errors are defined from the variance of results. The results on masses, widths, and photo-couplings are consistent with previously published values [85], and we refrain from a more detailed discussion.

We return to a discussion of the branching ratios. In the decays listed in Table 3 the phase space is rather different: the decay momentum for $\Delta(1950)7/2^+ \rightarrow N\pi$ is 730 MeV/c, the angular momentum between N and π is $L = 3$. The branching fraction is nevertheless very large. $\Delta(1920)3/2^+$ decays into $N\pi$ with about the same decay momentum but an angular momentum between N and π of $L = 1$ is sufficient. The angular momentum does not seem to be the decisive quantity which governs the decay. For $\Delta(1920)3/2^+ \rightarrow \Delta(1232)\eta$, the decay momentum is 335 MeV/c; this decay fraction is nevertheless of the same order of magnitude as that for its decay into $N\pi$. Also the linear momentum has not a highly significant impact on the decay branching ratios. The decay into $\Delta(1232)\eta$ requires an S -wave for $\Delta(1940)3/2^-$, a P -wave for $\Delta(1910)1/2^+$, $\Delta(1920)3/2^+$, and $\Delta(1905)5/2^+$. The latter three decay branching ratios are of similar magnitudes as the former ones. On average, the different branching ratios are of similar size, at least, there seems to be no large suppression of decay modes due to phase space or angular momentum barrier factors. We notice, however, that some resonances prefer decays into πN , in other cases, cascade decays are equally important. For the resonances

$$\begin{aligned} &\Delta(1700)3/2^- \quad \Delta(1910)1/2^+ \\ &\Delta(1920)3/2^+ \quad \Delta(1905)5/2^+ \quad \Delta(1950)7/2^+ \end{aligned} \quad (45)$$

the decay branching ratios to πN is larger than the branching ratios for decays into $N(1535)1/2^-\pi$. For all nucleon resonances and for $\Delta(1940)3/2^-$ the reverse is true; they prefer cascade decays to ground state transitions. The $N(1535)1/2^-\pi$ decay mode is not observed for the resonance $\Delta(1900)1/2^-$; we predict that it has a large coupling to $N(1520)3/2^-\pi$.

A similar observation has been made in $p\bar{p}$ annihilation: $p\bar{p}$ annihilation prefers to produce high mass and not high momentum [86]; there is little or no dependence of the decay branching ratios for $p\bar{p}$ annihilation into two mesons on the linear or orbital angular momentum between the two mesons produced in the process [87]. It may be illustrative to remind the reader that not all decay processes show a preference for high momenta. A well known example is the ejection of an electron of an excited atom: the Auger-Meitner process [88,89] preferentially ejects electrons of low kinetic energies.

The puzzling results on decay modes require detailed theoretical studies and may be a key to shed light on the structure of excited nucleon and delta resonances. As in atomic and nuclear spectroscopy the transition rates may be much more sensitive to the intrinsic structure of excited states. In quark models, the resonances listed in (45) have a comparably simple spatial wave function [34]. In the harmonic oscillator approximation, the excited states are represented by excitations of two oscillators λ and ρ . Two ex-

citations are possible, orbital (l_i , $i = \rho, \lambda$) and radial (n_i) excitations. The resonances listed in (45) have spatial wave functions which contain only components in which either λ or ρ carry one kind of excitation. In $\Delta(1900)1/2^-$ and $\Delta(1940)3/2^-$ both l and n are excited, in $\Delta(1700)3/2^-$ only l . In the four positive-parity $\Delta(1232)$ states, either ρ or λ carries two units of excitation, while $N(1900)3/2^+$ has, very likely [37], a wave function in which both oscillators l_ρ and l_λ carry one unit of excitation. Possibly, baryon resonances in a complicated excitation mode prefer to cascade down by de-excitation of one oscillator with subsequent de-excitation to the ground state. Clearly, more examples are needed to support or reject this conjecture.

8 Summary

We have reported a study of the reaction $\gamma p \rightarrow p\pi^0\eta$ for photon energies ranging from the threshold up to 2.5 GeV. After a detailed presentation of the experiment and of the selection of the final state, the data are presented in the form of Dalitz plots. The Dalitz plots reveal several contributing isobars: traces from $\Delta(1232)\eta$, $N(1535)1/2^-\pi$, and $pa_0(980)$ can be identified clearly. Angular distributions are presented in the center-of-mass system, in the Gottfried-Jackson and in the helicity frame. In the low-energy region the data are compared with the data from Mainz on the same reaction. Very good consistency was achieved.

Part of the data were taken with linearly polarized photons. This allowed us to extract several polarization variables: the conventional beam asymmetry Σ ; in a three-body final state Σ can be determined with respect to the three final-state particles. Exploiting the full three-body kinematics, two further variables can be deduced, I^s and I^c , which characterize the spin-alignment of the intermediate state when a linearly polarized photon is absorbed.

The new data are included in the database of the BnGa partial wave analysis. As three-body final state, they enter the program event-by-event in a likelihood fit. The fit returned masses, widths, and photo-couplings of four nucleon and seven Δ resonances compatible with previous results, and it returned decay modes of these resonances into $\Delta(1232)\eta$, $N(1535)1/2^-\pi$, $pa_0(980)$, and $N\pi$. It is conjectured that strong cascade decays like $N(1900)3/2^+ \rightarrow N(1535)1/2^-\pi \rightarrow N\pi\eta$ (and weak $N\pi$ decays) signal a non-trivial structure of the wave function of a decaying baryon resonance.

Acknowledgements

We thank the technical staff at ELSA and at all the participating institutions for their invaluable contributions to the success of the experiment. We acknowledge support from the Deutsche Forschungsgemeinschaft (within the SFB/TR16), the U.S. National Science Foundation (NSF), and from the Schweizerische Nationalfonds. The collaboration with St. Petersburg received funds from DFG and the Russian Foundation for Basic Research. This work comprises part of the PhD thesis of E. Gutz.

References

1. R. G. Edwards *et al.*, Phys. Rev. D **84**, 074508 (2011).
2. V. V. Anisovich, M. A. Matveev, V. A. Nikonov, J. Nyiri and A. V. Sarantsev, "Mesons and baryons: Systematization and methods of analysis," *Hackensack, USA: World Scientific (2008) 580 p.*
3. E. Klempt and A. Zaitsev, Phys. Rept. **454**, 1 (2007).
4. See, e.g., E. Klempt and J. M. Richard, Rev. Mod. Phys. **82**, 1095 (2010).
5. S. Capstick and N. Isgur, Phys. Rev. D **34**, 2809 (1986).
6. L. Y. Glozman, W. Plessas, K. Varga and R. F. Wagenbrunn, Phys. Rev. D **58**, 094030 (1998).
7. U. Loring, B. C. Metsch and H. R. Petry, Eur. Phys. J. A **10**, 395 (2001).
8. U. Loring, B. C. Metsch and H. R. Petry, Eur. Phys. J. A **10**, 447 (2001).
9. S. Capstick and P. R. Page, Phys. Rev. C **66**, 065204 (2002).
10. J. J. Dudek and R. G. Edwards, Phys. Rev. D **85**, 054016 (2012).
11. O. Krehl, C. Hanhart, S. Krewald, and J. Speth, Phys. Rev. C **62**, 025207 (2000).
12. I. G. Aznauryan *et al.*, Phys. Rev. C **78**, 045209 (2008).
13. E. Santopinto and M. M. Giannini, Phys. Rev. C **86**, 065202 (2012).
14. L. Y. Glozman, Phys. Lett. B **587**, 69 (2004).
15. L. Y. Glozman, Phys. Lett. B **475**, 329 (2000).
16. P. Bicudo, M. Cardoso, T. Van Cauteren and F. J. Llanes-Estrada, Phys. Rev. Lett. **103**, 092003 (2009).
17. R. L. Jaffe, Phys. Rept. **409**, 1 (2005) [Nucl. Phys. Proc. Suppl. **142**, 343 (2005)].
18. L. Y. Glozman, Phys. Rept. **444**, 1 (2007).
19. L. Y. Glozman and A. V. Nefediev, Nucl. Phys. A **807**, 38 (2008).
20. D. Berenstein, C. P. Herzog and I. R. Klebanov, JHEP **0206**, 047 (2002).
21. S. J. Brodsky and G. F. de Teramond, Phys. Rev. Lett. **96**, 201601 (2006).
22. F. Wilczek, "Diquarks as inspiration and as objects," In *Shifman, M. (ed.) et al.: From fields to strings, vol. 1* 77-93 [hep-ph/0409168].
23. H. Forkel and E. Klempt, Phys. Lett. B **679**, 77 (2009).
24. S. Weinberg, Physica A **96**, 327 (1979).
25. V. Bernard, N. Kaiser and U.-G. Meißner, Int. J. Mod. Phys. E **4**, 193 (1995).
26. M. F. M. Lutz, G. Wolf and B. Friman, Nucl. Phys. A **706**, 431 (2002) [Erratum-ibid. A **765**, 431 (2006)].
27. M. Bando, T. Kugo, S. Uehara, K. Yamawaki and T. Yanagida, Phys. Rev. Lett. **54**, 1215 (1985).
28. E. Oset *et al.*, Prog. Theor. Phys. Suppl. **186**, 124 (2010).
29. G. Höhler *et al.*, "Handbook Of Pion Nucleon Scattering," Fachinform. Zentr. Karlsruhe 1979, 440 P. (Physics Data, No.12-1 (1979)).
30. R. E. Cutkosky *et al.*, "Pion - Nucleon Partial Wave Analysis," 4th Int. Conf. on Baryon Resonances, Toronto, Canada, Jul 14-16, 1980. Published in Baryon 1980:19 (QCD161:C45:1980).
31. R. A. Arndt *et al.*, Phys. Rev. C **74**, 045205 (2006).
32. A. V. Anisovich, R. Beck, E. Klempt, V. A. Nikonov, A. V. Sarantsev and U. Thoma, Eur. Phys. J. A **48**, 15 (2012).
33. A. V. Anisovich, E. Klempt, V. A. Nikonov, A. V. Sarantsev, H. Schmieden and U. Thoma, Phys. Lett. B **711**, 162 (2012).
34. E. Klempt and B. C. Metsch, Eur. Phys. J. A **48**, 127 (2012).
35. V. Crede and W. Roberts, Rept. Prog. Phys. **76**, 076301 (2013).
36. M. Anselmino, E. Predazzi, S. Ekelin, S. Fredriksson and D. B. Lichtenberg, Rev. Mod. Phys. **65**, 1199 (1993).
37. A. V. Anisovich, E. Klempt, V. A. Nikonov, A. V. Sarantsev and U. Thoma, Phys. Lett. B **711**, 167 (2012).
38. I. Horn *et al.*, Eur. Phys. J. A **38**, 173 (2008).
39. I. Horn *et al.*, Phys. Rev. Lett. **101**, 202002 (2008).
40. V. Sokhoyan *et al.*, "High statistics study of the reaction $\gamma p \rightarrow p 2\pi^0$ ", in preparation.
41. C. Weinheimer *et al.*, Nucl. Phys. A **721**, 781 (2003).
42. G.F. de Teramond and S.J. Brodsky, Phys. Rev. Lett. **94**, 201601 (2005).
43. A. Karch, E. Katz, D.T. Son and M.A. Stephanov, Phys. Rev. D **74**, 015005 (2006).
44. H. Forkel, M. Beyer and T. Frederico, JHEP **0707**, 077 (2007).
45. For a survey on light-front dynamics and AdS/QCD, see S.J. Brodsky and G.F. de Teramond, PoS LC **2010**, 070 (2010), and references therein.
46. J. Ajaka *et al.*, Phys. Rev. Lett. **100**, 052003 (2008).
47. V.L. Kashevarov *et al.*, Eur. Phys. J. A **42**, 141 (2009).
48. W. Roberts and T. Oed, Phys. Rev. C **71**, 055201 (2005).
49. E. Gutz *et al.*, Phys. Lett. B **687**, 11 (2010).
50. M. Döring, E. Oset and U.-G. Meißner, Eur. Phys. J. A **46**, 315 (2010).
51. M. Döring, E. Oset and D. Strottman, Phys. Rev. C **73**, 045209 (2006).
52. W. Hillert, Eur. Phys. J. A **28S1**, 139 (2006).
53. E. Aker *et al.*, Nucl. Instrum. Meth. A **321**, 69 (1992).
54. R. Novotny, IEEE Trans. Nucl. Sci. **38**, 379 (1991).
55. A.R. Gabler *et al.*, Nucl. Instrum. Meth. A **346**, 168 (1994).
56. D. Elsner *et al.*, Eur. Phys. J. A **39**, 373 (2009).
57. F.A. Natter, P. Grabmayr, T. Hehla, R.O. Owens and S. Wunderlich, Nucl. Instrum. Meth. B **211**, 465 (2003).
58. D. Elsner, *Untersuchung kleiner Partialwellenbeiträge in der Nähe dominierender Resonanzbeiträge des Protons mit linear polarisierten Photonen*, PhD thesis, Physikalisches Institut, Universität Bonn, 2007.
59. G. Suft *et al.*, Nucl. Instrum. Meth. A **538**, 416 (2005).
60. A. Fösel, *Entwicklung und Bau des Innendetektors für das Crystal Barrel Experiment an ELSA/Bonn*, PhD thesis, Physikalisches Institut, Universität Erlangen, 2001.
61. O. Bartholomy, *Test und Modifikation des Lichtpulser-systems für den CB-ELSA-Detektor*, Diploma thesis, Helmholtz-Institut für Strahlen- und Kernphysik, Universität Bonn, 2000.
62. S. Janssen, *Entwicklung eines CPV-Systems für TAPS*, Diploma thesis, II. Physikalisches Institut, Universität Giessen, 1998.
63. J. Junkersfeld, *Kalibration des Crystal Barrel-ELSA Detektors mit Hilfe der Reaktion $\gamma p \rightarrow p\pi^0$* , Diploma thesis, Helmholtz-Institut für Strahlen- und Kernphysik, Universität Bonn, 2000.
64. R. Castelijns, *Photoproduction of strange mesons and hyperons in the proton*, PhD thesis, Rijksuniversiteit Groningen, 2006.

65. H. van Pee *et al.*, Eur. Phys. J. A **31**, 61 (2007).
66. V. Crede *et al.*, Phys. Rev. C **84**, 055203 (2011).
67. E. Gutz *et al.*, Eur. Phys. J. A **35**, 291 (2008).
68. R.P. Worden, Nucl. Phys. B **37**, 253 (1972).
69. A. Fix and H. Arenhövel, Phys. Rev. C **83**, 015503 (2010).
70. M. Döring, C. Hanhart, F. Huang, S. Krewald and U.-G. Meißner, Phys. Lett. B **681**, 26 (2009).
71. M. Döring, C. Hanhart, F. Huang, S. Krewald and U.-G. Meißner, Nucl. Phys. A **829**, 170 (2009).
72. N. Kaiser, P. B. Siegel and W. Weise, Phys. Lett. B **362**, 23 (1995).
73. U.-G. Meißner and J. A. Oller, Nucl. Phys. A **673**, 311 (2000).
74. J. Nieves and E. Ruiz Arriola, Phys. Rev. D **64**, 116008 (2001).
75. A.V. Anisovich, E. Klempt, A.V. Sarantsev and U. Thoma, Eur. Phys. J. A **24**, 111 (2005).
76. A.V. Anisovich and A.V. Sarantsev, Eur. Phys. J. A **30**, 427 (2006).
77. J.M. Blatt, V.F. Weisskopf, *Theoretical nuclear physics*, Wiley, 1952.
78. A. V. Anisovich, R. Beck, E. Klempt, V. A. Nikonov, A. V. Sarantsev and U. Thoma, Eur. Phys. J. A **48**, 88 (2012).
79. S. U. Chung, J. Brose, R. Hackmann, E. Klempt, S. Spanier and C. Strassburger, Annalen Phys. **4**, 404 (1995).
80. R. L. Workman, L. Tiator and A. Sarantsev, Phys. Rev. C **87**, 068201 (2013).
81. U. Thoma, M. Fuchs, A. V. Anisovich, G. Anton, R. Bantes, O. Bartholomy, R. Beck and Y. Beloglazov *et al.*, Phys. Lett. B **659**, 87 (2008).
82. A.V. Anisovich, E. Klempt, V.A. Nikonov, A.V. Sarantsev and U. Thoma, Eur. Phys. J. A **47**, 27 (2011).
83. A.V. Anisovich, E. Klempt, V.A. Nikonov, A.V. Sarantsev and U. Thoma, Eur. Phys. J. A **47**, 153 (2011).
84. A. V. Anisovich, E. Klempt, V. A. Nikonov, A. V. Sarantsev and U. Thoma, accepted for publication in EPJ A, arXiv:1310.3610 [nucl-ex].
85. J. Beringer *et al.* [Particle Data Group Collaboration], Phys. Rev. D **86**, 010001 (2012).
86. J. Vandermeulen, Z. Phys. C **37**, 563 (1988).
87. E. Klempt, C. Batty and J.-M. Richard, Phys. Rept. **413**, 197 (2005)
88. P. Auger, Journal de Physique et Le Radium **6**, 205 (1925).
89. L. Meitner, Zeitschrift fr Physik A **11**, 35 (1922).